Spring 2021

Numerical behavior of steel H-plies repaired using layered concrete jacket

Fareh Waleed Abudawaba

Department:

NUMERICAL BEHAVIOR OF STEEL H-PLIES REPAIRED USING LAYERED CONCRETE JACKET

by

FAREH WALEED ABUDAWABA

A THESIS

Presented to the Graduate Faculty of the

MISSOURI UNIVERSITY OF SCIENCE AND TECHNOLOGY

In Partial Fulfillment of the Requirements for the Degree

MASTER OF SCIENCE IN CIVIL ENGINEERING

2021

Approved by:

Mohamed A. ElGawady, Advisor
Grace Yan
Aditya Kumar

PUBLICATION THESIS OPTION

This thesis consists of the following two articles, formatted in the style used by the Missouri University of Science and Technology:

Paper I, found on pages 13–50, has been submitted for publication to *Transportation Research Record, Journal of the Transportation Research Board Journal*.

Paper II, found on pages 51–74, is under preparation and will be submitted to the *Journal of ASCE Bridge Engineering.*

ABSTRACT

This study developed finite element models (FEMs), using LS-Dyna software, to investigate the repair of corroded steel H-piles using concrete jacket. The concrete modeled as a layered material simulating 3D printed concrete. 3DPC is a new technology that can be used to repair or build structures without formwork by depositing concrete mixture layer by layer. For the 3DPC, this study investigated the feasibility of using alkali-activated concrete (AAC) synthesized using class C fly ash as the main binder. The fresh properties, extrudability, and buildability of the proposed concrete were investigated through open time and deformation tests, respectively. Hardened properties were also investigated through compressive strength. The effect of different cycle times (CTs) between subsequent layers and the effect of the loading direction on the compressive strength were investigated. Furthermore, a microstructural analysis was conducted to evaluate the bond area for a better understanding of the bond between subsequent layers. The developed mixtures had open time ranging from 2.5 to 31 minutes. The axial strain due to the deposition of concrete ranged from 0.17 to 11.2%. In terms of compressive strength, increasing the CT decreased the compressive strength of the 3DPC specimens. Anisotropic behavior was observed for 3DPC specimens tested in different directions. Microstructural analysis showed relatively high and low bond strength between layers having short and long CT, respectively. The FEMs showed that the behavior and the axial capacity of steel H-pile repaired with either 3DPC or traditional concrete were relatively close, which indicated that 3DPC using AAC has the potential to be used for repairing steel H-piles.

ACKNOWLEDGMENTS

First and above all, I praise God for providing me this opportunity and granting me the capability to proceed successfully. I would like to extend a special thanks to my advisor, Dr. Mohamed ELGawady, for his support, advice, guidance, and for sharing his knowledge that I needed. He always encouraged me to work hard and without his valuable advice and inputs, I would not be able to go that far. I would also like to thank Dr. Aditya Kumar and Dr. Grace Yan for being my committee members and providing suggestions, valuable knowledge, and support throughout my study.

I would also like to thank Dr. Ahmed Gheni, and Dr. Mohanad Abdulazeez for their patience, help, and support. A special shout-out to the students and staff in the Civil Engineering department: Eslam Gomaa, Binod Shrestha, Tousif Mahmood, Mashfiqul Islam, and Alireza Pourhassan for their help, support, and advice. Thanks also to Leckrone Ronald and John Bullock who helped me in the lab and offered a tremendous amount of technical assistance and support.

In closing, from all of my heart, I would also like to express my gratitude and deepest appreciation to my lovely husband for his great patience, support, and understanding, without his encouragement, I could not have finished this work. A special thanks to my parents who taught me a lot in my life for providing me with their love and prayers. Finally, I would like to express my unlimited and unconditional love to my son, Abdallah, who enlightened my life with his love and smile every day.

TABLE OF CONTENTS

LIST OF ILLUSTRATIONS

SECTION Page

LIST OF TABLES

1. INTRODUCTION

1.1. RESEARCH OVERVIEW

3D printing is a new technology process that can build a complex shape layer by layer where intricate shapes are printed layer by layer using computer-aided design software (Gao et al. 2015; Xia et al. 2019). 3D printing is also defined by the American Society for Testing and Materials as “the fabrication of objects through the deposition of a material using a print head, nozzle, or another printing technology (ASTM-F2792-10). 3D-printing is commonly known as additive manufacturing, digital fabrication, and rapid prototyping (ASTM-F2792-10 ; Tay et al. 2017). Nowadays, 3D printing is considered an important technology that is widely applied and found to have multiple successful applications in different areas such as aerospace, medical, biological, and construction industries (Ngo et al. 2018). Therefore, investigations into using 3D printing have expanded and are rapidly increasing.

The application of the 3D printing concrete (3DPC) industry has many significant advantages compared to conventional concrete which includes reducing the construction cost through cutting, construction time, workmanship, and formwork costs as well as the waste of the construction materials (Bong et al. 2018; Hager et al. 2016). Automated construction can benefit the construction sector significantly since more than 60% of the total cost of a new concrete construction project is spent on workmanship, and material (Jha 2012). In addition, 3D printing technology can build objects with high precision and very complicate geometry (Figure 1.1) since it is a very accurate construction machine as compared to the traditional formwork system (Malaeb et al. 2015; Xia et al. 2019). Thus,

columns, precast structures, houses, and walls with different shapes could be built by using 3DPC (Ma et al. 2018).

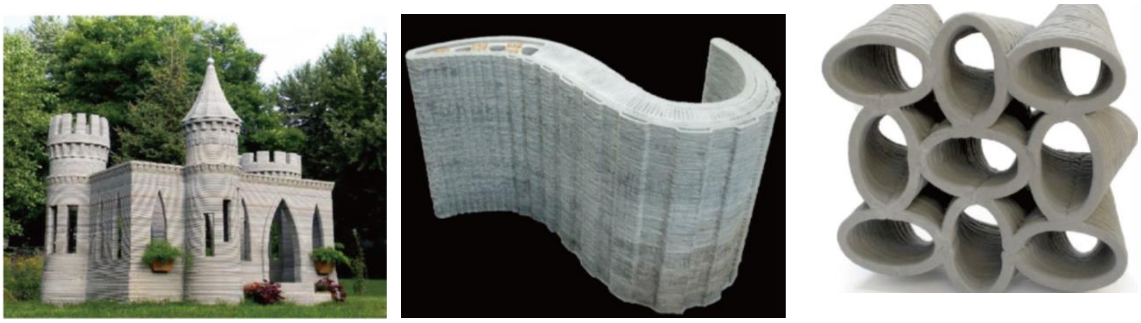

Figure 1.1: Examples of full-scale buildings using 3D printing.

Recently, different cementitious materials were used to create 3D, structures including either ordinary Portland cement concrete (OPC) (Kazemian et al. 2017; Le et al. 2012) or alkaline activated concrete (AAC) (Panda et al. 2017; Panda et al. 2017). AAC which also known as geopolymer concrete is an innovative material and alternative option of the OPC where there is no cement used in it (Davidovits 2013). AAC can be synthesized by the chemical reaction, which is called geopolymaraization reaction, between the source of silica and alumina, and alkaline activators (Davidovits 2013). A byproduct materials such as fly ash (FA) and ground granulated blast furnace slag (Duxson and Provis 2008; Nematollahi et al. 2018), which involve silica and alumina, are suitable for geopolymer production. It is worth noting that AAC doesn't depend on calcium carbonate as the main component which emits a large amount of carbon dioxide emissions during the manufacturing process, AAC is considered an environmentally

friendly material since it emits much less carbon dioxide compared to the OPC (Khan et al. 2020).

Steel H-piles is considered the main common structural system in bridge construction through the U.S. 65,000 bridges are deteriorated (FHWA 2015) due to the harsh environmental conditions including freeze-thaw cycles, deicing salt exposure, and increases in the applied loads as well. Thus, many of the steel H-piles are suffering from severe corrosion. Missouri is considered the seventh-largest state in terms of the number of bridges (Abdulazeez et al. 2019). Thus, the Missouri Department of Transportation (MoDOT) is addressing the repair and replacement of these deficient bridges. Different repairing methods were implemented by DOTs (Abdulazeez et al. 2019; Dawood et al. 2017; Wipf et al. 2003) to restore the original axial carrying capacity of corroded steel H-piles and subsequently strengthen the H-piles. Recently, researchers used a confined concrete jacket (Ehsani 2009; Karagah et al. 2018; Liu et al. 2001) or adding steel plates (Wan et al. 2013) for repair purposes. One of the new techniques that could be promised and has the potential for repair is 3D-printing. By applied layered concrete around the corroded region of the steel H-piles, the layered concrete encasement can serve as an alternative load path for the applied axial load. Thus, in this study, numerical finite element models were developed to investigate the behavior of the repaired steel H-piles encased with layered concrete.

1.2. OBJECTIVES

The main objectives of this study could be summarized into several points:

- Investigate the applicability of using class C FA based geopolymer mortar toward 3DPC.
- Propose and develop new test methods to evaluate the fresh properties including extrudability and buildability in terms of open time and deformation tests.
- Investigate the compressive strength of layered specimens and compare them with full caste specimen
- Conducted SEM analysis for a better understanding of the bond area between subsequent layers.
- Provide wide mixing proportions of class C FA through studying the effect of water to FA (W/FA), alkaline activators (i.e. sodium silicate and sodium hydroxide) to FA (Alk/FA), sodium silicate to sodium hydroxide (SS/SH) ratios.
- Analyze and evaluate a simple analytical model of corroded H-pile steel encased with 3D-printing layers and compare it with H-pile encased with a full layer using an advanced finite element software; LS-DAYNA.

1.3. METHODOLOGY

This research investigated the feasibility of using class C FA for different 3D printing applications through studying the effect of W/FA, Alk/FA, and SS/SH ratios. Extrudability and buildability were evaluated by conducting open time and deformation

tests, respectively. Newly proposed tests were developed to investigate the open time and deformation tests. Hardened properties including compressive strength, slant shear, tensile strength, and SEM analysis were investigated for 3DPC specimens and compared with full specimens as well. In addition, LS-DAYNA software was used to analyze the behavior of corroded H-piles steel encased with layered mortar to simulate 3D printing and compare it with corroded H-plie encased with full layered mortar.

2. LITERATURE REVIEW

3D printing is a new emerging technology and it considers one of the most advanced manufacturing processes. In order to build upon other ongoing researches, it is important to understand the concepts related to the 3DPC. The literature revealed that concrete based OPC is common as the main binder in 3D printing and a few were focused on the 3D printing based alkali-activated concrete. In this section, a comprehensive search was conducted on the literature review of the 3DPC area.

2.1. FRESH PROPERTIES OF 3DPC

As mentioned previously, 3DPC doesn't require formwork, therefore material deposition should be workable enough to avoid the blockage in the hosepipe so materials can be extruded from the nozzle easily. However material needs to set quickly to support itself and the other subsequent layers to maintain its shape without collapse or excessive deformation. Thus, extrudability and buildability should be studied and evaluated for producing successful mixtures for 3DPC applications. Extrudability is considered as a function of the open time which is defined as the suitable time interval at which the material can easily be transported from the pump to the extrusion nozzle without blockage in the hosepipe (Le et al. 2012; Malaeb et al. 2015). Thus it is important to optimize the mix design since it has a significant effect on printing to achieve a high quality of printing. Retarder (Le et al. 2012; Malaeb et al. 2015) and accelerator (Kazemian et al. 2017) were used to adjust the open time for 3DPC based OPC while

alkaline activators (i.e. sodium silicate, potassium silicate, and sodium hydroxide) (Kashani and Ngo 2018; Panda and Tan 2018) were used for 3DPC based geopolymer.

There was no standard method to evaluate the buildability where researchers evaluated it in many different ways (Ma et al. 2018; Malaeb et al. 2015; Nematollahi et al. 2018; Papachristoforou et al. 2018). First, it was evaluated by determining the maximum number of printable layers without collapse with a five target number of layers (Malaeb et al. 2015; Papachristoforou et al. 2018). Second, a thickness ratio of 1.0 between the first layer, and the fifth layer was targeted (Papachristoforou et al. 2018). It was concluded that with increasing the superplasticizer content (i.e. increasing the workability) of 3DPC based OPC, the buildability was hard to be achieved and higher deformation was observed (Malaeb et al. 2015; Papachristoforou et al. 2018). Third, in a 3DPC based OPC, copper tailing was partially replaced with sand to produce an environmentally friendly material with maximum cost-effective potentials (Ma et al. 2018). The buildability was evaluated by measuring the strain (i.e., vertical deformation to the optimal height) and the height to width ratio of twenty target number of layers (Ma et al. 2018). With increasing the copper tailing/sand, the twenty layers showed a higher strain and lower height to width, subsequently, poorer printable mixtures (Ma et al. 2018). Furthermore, one of the significant factors that influenced the buildability is the cycle time (i.e., time gap, paste age, delay time). The CT is defined as the time between placing a layer on top of another layer. With increasing the CT, the buildability improved where lower strain in the layer was observed, however, long CT affects the strength of the 3DPC specimens negatively (Zhang et al. 2018). Thus, this study investigated the fresh properties in terms of the open time and deformation tests and subsequently

evaluated the extrudability and buildability. Moreover, new proposed tests were developed to carry out these tests. W/FA. Alk/FA, and SS/SH were studying to develop a wide mix proportions that could be used for different 3DPC applications.

2.2. HARDENED PROPERTIES OF 3DPC

Since the 3DPC structure is built layer by layer, different studies were conducted to investigate the compressive strength in a different direction (i.e. the effect of loading direction on 3DPC specimens). Anisotropic behavior (i.e. the compressive strength is different when it is measured in a different direction) was reported for 3DPC based either OPC (Le et al. 2012; Ma et al. 2019; Marchment et al. 2017; Sanjayan et al. 2018) or AAC (Le et al. 2012; Nerella et al. 2019; Panda et al. 2017; Panda et al. 2017; Paul et al. 2018). While another study found the isotropic behavior of 3DPC specimen-based OPC (Rahul et al. 2019). Moreover, the compressive strength of 3DPC specimens was compared with full specimens. It was found that the compressive strength of 3DPC specimens was less than the full specimens (i.e. one pouring) (Le et al. 2012; Rahul et al. 2019). For example, the compressive strengths for 3DPC specimens were lower by 5-15% than those of full specimens [33]. This reduction was explained due to the void existing between subsequent layers. On the other hand, it was found that the compressive strength of full specimens was lower by 15% than 3DPC specimens due to the effect of the printing parameters such as printing pressure, speed, and nozzle diameter [40] the Thus, these observed results were contradictory and a further study is needed.

Bond strength is a key factor in the stability of 3D printed structures. To obtain an optimum compressive strength and guarantee the stability of the structures, sufficient

bond strength is required between subsequent layers. Thus, a tensile test was conducted on 3DPC specimens to investigate the bond strength (i.e., adhesion between layers). One of the factors that affect bond strength is the CT between layers. It was observed that with increasing the CT between layers, the bond strength of 3DPC specimens-based AAC decreased [41]. This result agreed with the other observations of 3DPC specimens based-OPC (Le et al. 2012; Tay et al. 2019). As the CT increases, more nucleation occurs between either 3DPC based OPC or based AAC which subsequently improves the overall layer stiffness, resulted in a weak bond due to the insufficient interaction between the layers (Le et al. 2012; Panda et al. 2017; Panda et al. 2018; Tay et al. 2019).

For a better understanding of the bond area between two subsequent layers, a few studies focused on the microstructural analysis of 3DPC at the interlayer interface using scanning electronic microscopy (SEM) (Kosson et al. 2020; Nerella et al. 2019). In SEM images of 3DPC specimens based OPC having a CT of 2 minutes, 10 minutes, or 24 hours, large cavities were observed and the separation was clear between two subsequent layers despite the higher flexural strength of 3DPC specimens having CT of either 2 or 10 minutes compared with 24 hours. By replacing 30% of OPC with FA by weight to the OPC, a stronger bond, and fewer cavities were observed in the two layers of 3DPC specimen having a CT of 2 minutes compared with those of 3DPC specimens having only OPC (Nerella et al. 2019). Another study found that there wasn't a distinctive change (i.e., cavities were observed between two subsequent layers) in the SEM images for different 3DPC specimens based OPC having either carbon microfibers or carbon nanofibers despite the higher compressive strength of 3DPC having carbon microfibers (Kosson et al. 2020). It is worth noting that none of these studies visualized either the

elemental line scan analysis for 3DPC specimens (Kosson et al. 2020; Nerella et al. 2019). Thus, this study investigated the SEM images and elemental line scan of the 3DPC specimens having different CTs for a better understanding of the bond strength between two subsequent layers.

2.3. REPAIRING STEEL H-PILES

Steel H-piles are widely used in bridge construction and offshore structures throughout the U.S. since steel H-piles carry a large amount of loads while occupying a relatively small area. Many of these H-piles, throughout their life service, suffer from the severing localized corrosion damage due to the environmental conditions including (i.e., repetitive dry-wet cycles) (Figure 2.1). For example, the Missouri Department of Transportation (MoDOT) is responsible for maintaining nearly 10,400 bridges on the state system since Missouri is the 4th highest state in terms of deficient bridges, with 3,222 deficient bridges (FHWA 2015). Many of these were constructed using steel H-piles as substructures. Thus, there is an urgent need to repair these piles using new techniques that have longer durability and require less maintenance during the extended service life of the bridge.

Different repair methods have been implemented by DOTs for strengthening and restoring the axial capacity of the corroded steel H-piles. Repairing involves steel channels bolted or welded to the exterior of the flange across the damaged area of the pile were used by IADOT (Wipf et al. 2003), GDOT (Georgia Department of Transportation 2012), WisDOT (Wan et al. 2013), and (Department of the Army 1991). This type of

repair would only serve as a temporary repair because of its susceptibility to continued corrosion (Stauffer 2016)

Figure 2.1: Corrosion of H-piles in I-70/I-270 interchange in St. Louis.

Another repair technique included the application of a concrete jacket (Figure 2.2) to corroded steel members to increase the strength of the corroded area. It is considered one of the most cost-effective and easy to implement repair techniques (Soliman et al. 2013). The form can remain in place as part of the jacket or can be removed, leaving the concrete on the repaired piling.

Recently, 3D printing technology has growing rabidly in industrial construction due to the significant advantages as compared to conventional concrete. It considers a new emerging technology that can build a structure by depositing materials layer by layer without formwork (Ngo et al. 2018). Thus, it has the potential to repair corroded steel H-pile steel by printing the layered concrete as a jacket around the corroded steel H-pile.

Figure 2.2: Concrete encasement repairing method (ODOT 2008).

To date 3D printing hasn't been implemented for repairing steel H-pile, thus, it better to understand the behavior of the corroded steel H-piles using the finite-element (FE) method. FE offers an approach to investigate and understand the behavior of such a new repair method using LS-DYNA software to simulate different models encased with layered concrete to mimic 3D printing.

PAPER

I. DEVELOPING MIX PROPORTIONS OF CLASS C FLY ASH BASED GEOPOLYMER MORTAR FOR USE IN SIMULATING 3D-PRINTING

ABSTRACT

This study investigated the use of class C fly ash (FA) as a precursor for geopolymer mortar mixtures for 3D-printing. Experimental tests were performed on different mixtures with varied proportions of precursors and activators to achieve the targeted fresh and hardness properties for potential use in specific 3D-printing applications. The fresh properties including extrudability and buildability were evaluated through open time and deformation tests, respectively. In addition, the ability of mortar specimens to carry the loads in different directions at different cycle time (CT) between the layers was examined as a way to evaluate the bond between the layers after comparing the results with the full specimen. To offer a wide selection of mixtures based on the targeted shape and strength of the 3D-printed element, water to FA (W/FA), Alkaline activator to FA (Alk/FA), sodium silicate to sodium hydroxide (SS/SH) ratios were varied and studied. The results revealed that the open time ranged from 2.5 minutes to 31 minutes. Different CTs were applied to avoid collapse and to reach the minimum strain necessary to enhance the buildability. The strain was ranged from 0.17 to 11.2% depending on the time selected to add the subsequent load which provides flexibility to select a suitable 3D-printed geopolymer mix depending on the targeted application. The results revealed 3D-printed specimens had anisotropic behavior compared with

conventional full specimens. In addition, the compressive strength of full specimens was higher by 0.2-18.4 % and 0.9-28 % than 3D-printed specimens tested in X and Z directions, respectively.

1. INTRODUCTION

3D-printing is a new technology that can be adopted for printing concrete structures in layers using computer-aided design software and digital model data (Gao et al. 2015; Ngo et al. 2018). Adopting 3D-printed concrete (3DPC) has many advantages compared to conventional concrete construction including the ability to print intricate shape structures as well as reducing the construction time, workmanship, formwork costs, and construction material waste which could lead to cost savings (Bong et al. 2018; Hager et al. 2016; Jha 2012; Malaeb et al. 2015).

The majority of research on 3DPC uses ordinary Portland cement (OPC)-based concrete (Alghamdi et al. 2019; Le et al. 2012; Le et al. 2012; Malaeb et al. 2015; Marchment et al. 2017; Mechtcherine et al. 2014; Nerella and Mechtcherine 2019; Paul et al. 2018; Rahul et al. 2019; Sanjayan et al. 2018; Wolfs et al. 2019). Recently, alkali-activated concrete (AAC), also called geopolymer concrete, was developed for 3DPC. AAC is synthesized by activating industrial byproduct materials such as fly ash (FA), or synthesized material such as metakaolin (Duxson and Provis 2008; Nematollahi et al. 2018). AAC has the potential to perform better than or equal to conventional concrete as the setting time can be tailored for different 3DPC applications (Gomaa et al. 2018; Gomaa et al. 2019; Nematollahi et al. 2018; Sanjayan 2016; Sumer 2012). Developing

AAC mixtures using byproduct materials also offers an eco-friendly alternative concrete material.

This manuscript focuses on FA-based alkali-activated mortar (AAM) for 3D printing. ASTM 618-15 (ASTM-C618 2015) classifies FA into two classes: class F and class C. Class F is commonly used as a precursor for AAC; recent studies, however, have successfully used class C FA as a precursor for AAC. While the former is cured at elevated temperatures, the later can be cured at the ambient or elevated temperatures while displaying compressive strength adequate for structural applications (Gomaa et al. 2018; Gomaa et al. 2020).

Various research projects were conducted on 3DPC to investigate its fresh properties including extrudability and buildability (Nerella and Mechtcherine 2019; Panda and Tan 2018; Paul et al. 2018; Zhang et al. 2018), and hardened properties including compressive and bond strengths (Feng et al. 2015; Panda et al. 2017; Paul et al. 2018; Sanjayan et al. 2018). Extrudability is measured by the open time which is defined as the time interval when the concrete mixture does not display discontinuity, disturbance, or signs of tearing of the filament. During that time, called the printability limit, concrete can easily be transported from the pump to the extrusion nozzle without blockage in the hosepipe (Kazemian et al. 2017; Le et al. 2012; Ma et al. 2018; Malaeb et al. 2015; Panda and Tan 2018). While printed concrete requires adequate open time to be extruded, it needs high early strength and rapid setting time in order to be buildable. Buildability refers to the ability of materials to resist the deformation and collapse under its own weight, i.e., shape stability (Ma et al. 2018; Ngo et al. 2018). In addition, the concrete should be viscous enough to bond to the subsequent layers to avoid the

formation of poor bond strength cold joints. Thus, it is important to balance and optimize these properties to ensure success in constructing a 3DPC structure.

Open times ranging from 10 minutes to 225 minutes were reported for AAM depending on the alkaline activator characteristics and slag content (Bong et al. 2018; Kashani and Ngo 2018; Panda and Tan 2018; Paul et al. 2018). Decreasing the ratio of sodium silicate activator from 10% to 8% per total mass of the precursor increased the open time from 60 minutes to 155 minutes due to the lower rate of the particles dissolution (i.e. lower rate of reaction) (Kashani and Ngo 2018). Changing from Na-based to k-based activators increased the open time from 15 minutes to 29 minutes due to the relatively slow rate of geopolymerization reaction of the Na-based activators (Bong et al. 2018). Moreover, increasing the slag content from 5% to15% of the FA mass resulted in a non-printable mixture since the slag increased the yield stresses from 0.86 to 1.04 KPa (Panda and Tan 2018).

There is no standard test to evaluate concrete buildability and different tests have been used for OPC-based (Ma et al. 2018; Malaeb et al. 2015; Papachristoforou et al. 2018) and AAC-based (Nematollahi et al. 2018) 3DPC. The maximum number of layers printed with a 20 mm diameter nozzle without collapse was proposed as a measure for buildability (Malaeb et al. 2015). Another proposed measure was to print five consecutive layers using a 20 mm nozzle diameter with no significant deformation in the bottom layer (Papachristoforou et al. 2018). It was concluded that by increasing the workability of OPC-based 3DPC, buildability was harder to achieve and higher deformation occurred (Malaeb et al. 2015; Papachristoforou et al. 2018). Another factor that affects influences buildability is the cycle time (CT) which is defined as the time between placing two

consecutive layers (i.e. gap time (Tay et al. 2019), delay time (Marchment et al. 2017), or paste age (Li et al. 2018)). CT ranging from 7 seconds to 6 hours was used for AAM- (Panda et al. 2017; Panda et al. 2018; Panda et al. 2017). As the CT increased, the buildability improved where lower strain in the layer was observed. However, a longer CT reduced the strength of the 3D-printed specimens (Li et al. 2018). As the CT increased the bond strength decreased due to the poly-condensation in AAC and poor bonding between layers since the layers hardened with increasing the CT (Panda et al. 2017; Panda et al. 2018).

The bond strength between consecutive layers is one of the factors that define the performance of the printed structure. The interlayer bond strength should be adequate to achieve the required compressive strength and guarantee the stability of the structure (Kazemian et al. 2017; Ngo et al. 2018; Panda et al. 2017; Paul et al. 2018; Sanjayan et al. 2018). AAC-based 3DPC displayed anisotropic behavior, i.e., the strength values are based on the direction of testing (Panda et al. 2017; Panda et al. 2017). The average compressive strength of AAC-based 3DPC specimens tested in parallel to the layer deposition was 5% higher than those tested perpendicular to the layer deposition. In contrast, another study found that the compressive strength of AAM-based 3D printed specimens tested in the perpendicular direction was 2 to 7 % higher than those tested in the parallel direction (Panda et al. 2017).

Both OPC-based (Alghamdi et al. 2019; Le et al. 2012; Le et al. 2012; Malaeb et al. 2015; Marchment et al. 2017; Mechtcherine et al. 2014; Nerella and Mechtcherine 2019; Paul et al. 2018; Rahul et al. 2019; Sanjayan et al. 2018; Wolfs et al. 2019) and a combination of class F FA and slag-based (Alghamdi et al. 2019; Bong et al. 2018;

Kashani and Ngo 2018; Panda et al. 2017; Panda and Tan 2018; Panda et al. 2018; Paul et al. 2018; Xia et al. 2019) concrete mixtures were developed for 3D printing. The results from some of these studies are conflicting. Furthermore, there are no studies on using class C FA-based AAC for 3DPC applications. Thus, this study was conducted to investigate the feasibility of using class C FA to simulate 3D printing. This study investigates the performance of nine class C FA-based AAM mixtures in simulating 3D printing. When reviewing past research it was found that there was no open time less than 10 minutes, thus using class C FA-based AAM has the potential to result in mortar mixtures with short open time (i.e. less than 10 minutes), which is important for different 3D printing applications. Open time was determined by using the flow table test. A new test setup was developed to evaluate the buildability by measuring the normal deformation. In addition, the compressive strengths of the developed mixtures were determined in two directions, i.e., parallel and perpendicular to layer disposition. Furthermore, the disposition of the multiple layers was carried out to simulate 3D printed specimens using a wide range of CTs that could be used for different 3D printing applications.

2. EXPERIMENTAL PROGRAM

2.1. MATERIALS PROPERTIES

2.1.1. Fly Ash (FA) and Sand. Class C FA per ASTM C618-15 (ASTM-C618 2015), was used as the precursor for the AAM in this study (Table 1). River sand with a

fineness module of 2.25 and a maximum particle size of 1.18 mm was used as a fine aggregate.

Table 1: Chemical composition of the FA using X-ray fluorescence (XRF).

Composition	SiO_2	Al_2O_3	Fe_2O_3	CaO	MgO	Na_2O	K_2O	TiO_2	P_2O_5	MnO	LOI*
wt.%	43.91	20.12	4.96	21.24	4.29	2.87	0.70	1.36	0.51	0.05	0.40

*Loss on ignition

2.1.2. Alkali Activators. Two types of alkali activators were used including sodium hydroxide (SH) and sodium silicate (SS) solutions. An SH solution having 10M was prepared and cooled to room temperature before use (Gomaa et al. 2017). The SS was in a solution form with 44.1% and 55.9% solids and water contents by weight, respectively. The SiO2/Na2O of the SS's solids was 2.0 (Yacob et al. 2019).

2.2. MIX DESIGN AND MIXING PROCEDURE

Nine AAM mixtures were prepared having different water to FA (W/FA), alkali activators to FA (Alk/FA), and SS/SH ratios. The W/FA ranged from 0.340 to 0.420, Alk/FA ranged from 0.250 to 0.300, and SS/SH ratio ranged from 0.5 to 2.0 (Table 2). The W/FA included both water in the alkaline activators and the extra water added during the mixing. The range of W/FA was selected to present a range of relatively stiff and flowable mixtures for different applications While the Alk/FA and SS/SH ranges were selected following (Gomaa et al. 2017; Gomaa et al. 2017; Yacob et al. 2019) since they displayed acceptable setting times and compressive strengths for AAM for the 3DPC process.

The mixing procedure was optimized following (Gomaa et al. 2021), and the materials were mixed as follows: FA and sand were mixed together for one minute and water was added over 1 minute. Then, the alkaline activators were mixed together before adding them gradually over two minutes. Finally, all the components were mixed together for another one minute. The mixing speed was fixed at 136 rpm.

Table 2: Mix design of AAM mixtures.

Mix no.	W/FA	Alk/FA	SS/SH	Sand	FA	SS	SH	Extra Water
1	0.34	0.300	1.0	1526	555	83.3	83.3	92.6
2	0.36	0.300	1.0	1513	550	82.5	82.5	102.8
3	0.38	0.300	1.0	1499	545	81.8	81.8	112.8
4	0.40	0.300	1.0	1471	535	80.3	80.3	121.4
5	0.42	0.300	1.0	1458	530	79.5	79.5	130.9
6	0.36	0.275	1.0	1513	550	75.6	75.6	111.3
7	0.36	0.250	1.0	1513	550	68.8	68.8	119.7
8	0.36	0.300	0.5	1513	550	55.0	110.0	99.8
9	0.36	0.300	2.0	1513	550	110.0	55.0	105.9

2.3. EXTRUDABILITY AND BUILDABILITY

Since there is no standard test for 3DPC, a modified mini-slump test, and non-standard deformation test were proposed to determine the open time and deformation as measures for extrudability and buildability, respectively. It is worth noting that open time and deformation tests were carried out on different specimens and both tests were performed at different intervals time.

2.3.1. Open Time. Open time, which is the time where is the AAM could be extruded and beyond it, the blockage would occur, was measured by conducting consecutive mini-slump tests at different time intervals after mixing until the mixture lost

its workability. A concrete mixture was mixed and left at rest in the mixing bowl for a given time; then, the AAM was placed in the standard ASTM C230 (ASTM-C230/230M 2008) brass cone without compaction to simulate 3DPC and the cone was lifted vertically leaving the mortar on a flow table. Then, the flow table was dropped 25 times in 15 seconds per ASTM C1437 (ASTM-C1437 2015). The process was repeated for the same mixture at increasing times until the mixture lost its workability (i.e., zero spread diameter of the AAM after dropping the flow table 25 times). That time was recorded as the open time. To accommodate mixtures with short open times, running three flow tables operated by different users were required (Figure 1a-c). The test was repeated four times for each mix design. The AAM which remained in the mixing bowl was remixed before used for the open time test to mimic 3DPC.

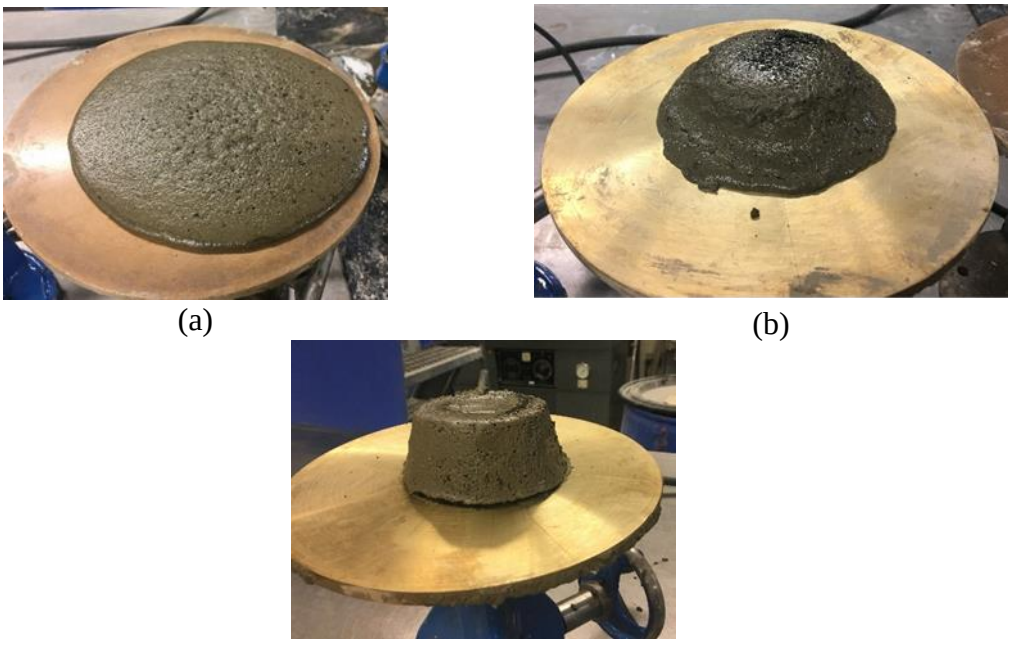

(a) (b)

(c)

Figure 1: Three flow tables to measure the spread diameter at different times for mixture M1 at (a) zero, (b) one and a half, and (c) two and half minutes after mixing.

2.3.2. Deformation Testing. Since there is no ASTM standard test for measuring the deformation for 3DPC, a testing method was developed (Figure 2). The test measures the axial deformation of a 700 gm mortar layer subjected to incremental axial loads representing the applied weight of the added mortar layers during 3D printing. The incremental load was applied at different CTs which is the time between adding the subsequent loads.

Four dial gages were attached to each corner of a 230 mm square plexiglass plate which was resting on an upright cylinder (Figure 2). A piece of non-absorbent butcher paper was placed on the plexiglass to increase surface friction (Figure 2a). A 150 mm diameter 15 mm high plastic ring beam having three legs was placed and centered on a plexiglass plate (Figure 2a). The legs were used to ensure the fixation of the ring into the plexiglass preventing its horizontal movement (Figure 2a). The ring was filled with 700 gm fresh mortar which was poured continuously and then the surface was flushed (Figure 2b). A vertical thin metal rod was continually centered on top of a plexiglass plate that was placed atop the mortar specimen and the dial gages measuring the spacing between the two plexiglass plates were zeroed (Figure 2c). The top plexiglass plate and the plastic ring beam were removed (Figure 2d). The top plexiglass was placed again atop of the mortar layer at the required CT and the axial deformation was measured (Figure 2e). The weight of the plexiglass plate with the rod was 700 gm which represented a weight equivalent to that of the used mortar layer (Figure 2e).

Seven-hundred grams, equivalent to the weight of a mortar layer representing the weight of the consecutive mortar layers, was added in increments to the top of the plexiglass plate at the required CT (Figure 2f). Each weight had a hole in its center where

it was installed on the rod atop of the plexiglass plate. The weights were added until the dial gauge readings remained constant. CTs of 1.0, 2.5, and 5.0 minutes were selected for mixtures having short open times of ten minutes or less and long open times as well. Short CTs could be a benefit for refabricated small structures, thus it is crucial to investigate the deformation for those short CTs. Likewise, for mixtures having a longer open time, CTs of 30 and 60 minutes were used to offer a wide range of options for different applications of 3DPC such as a house. The average deformation obtained using the four dial gages was determined and converted to axial strains. The entire procedure was repeated for each selected CT for a mixture It is worth noting that this test was carried out under controlled conditions for each selected CT; the temperature and relative humidity was 23 ± 2o C and 60%, respectively.

In summary, the logic behind the deformation test was to simulate the reality of 3D-printing by adding a load having the same weight as the mortar. Besides, within the deformation test, the load was applied at different CTs since CT is considered a significant factor that affects the deformation.

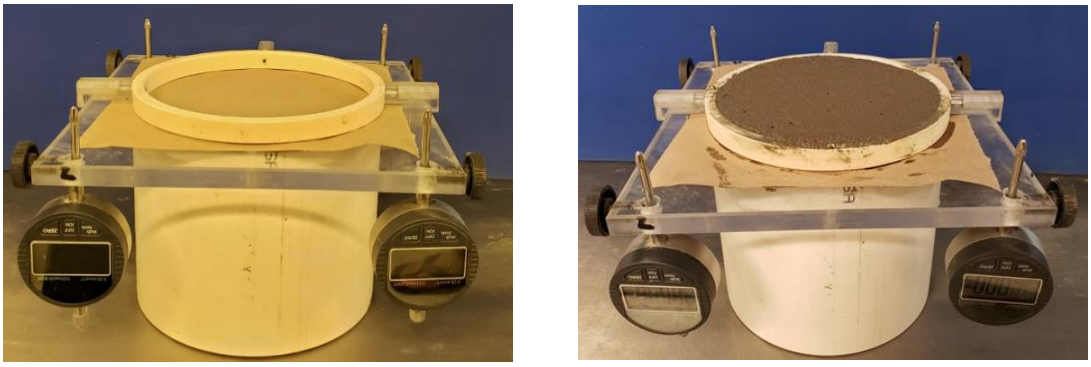

(a) (b)

Figure 2: Deformation measurement setup attached with four dial gages.

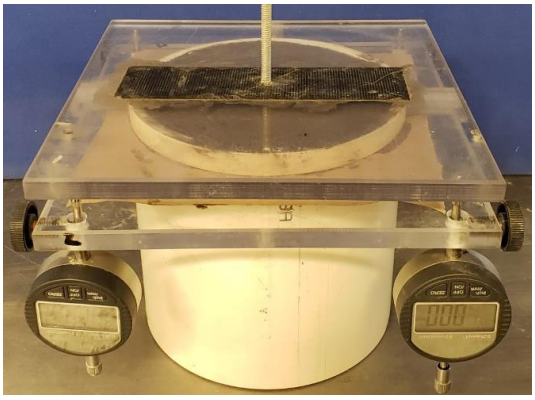

(c)

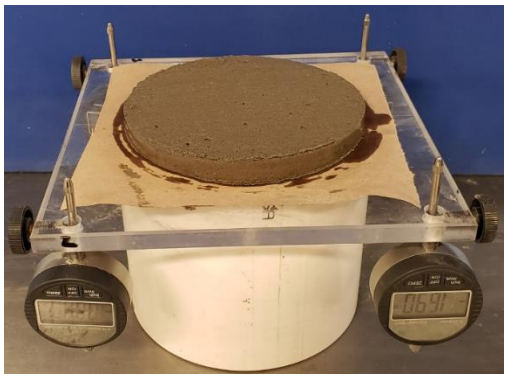

(d)

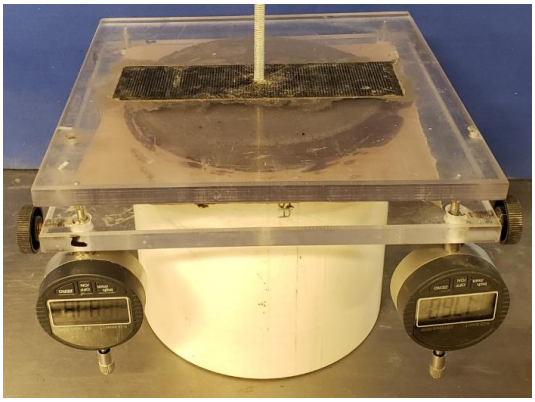

(e)

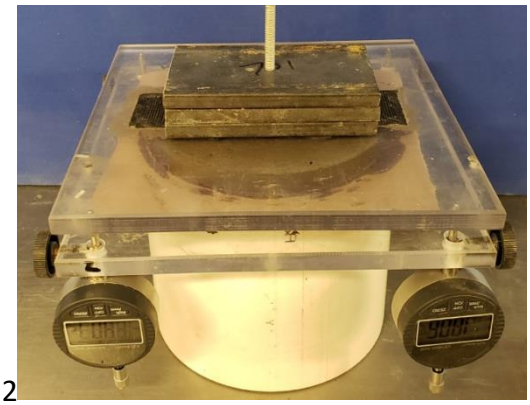

2

(f)

Figure 2: Deformation measurement setup attached with four dial gages (cont.).

2.4. COMPRESSIVE STRENGTH AND MICROSTRUCTURAL ANALYSIS

2.4.1. Effect of the Loading Direction on the Compressive Strength. For each mixture, the fresh mortar was cast in three 50 mm brass cubic molds. Since no actual 3D-printing was carried out in this study, two types of specimens were cast to simulate 3D-printing: full cube casting on one pouring (Figure3a) and casting of mortar in four layers with different CTs between layers (Figure3a). A layer specimen 12.5 mm thick was cast to simulate the 3DPC process (Figure 3). The full specimens were used as reference specimens for comparison purposes. It is worth noting that although the ASTM C109-16

(ASTM-C109/C109M 2016) requires the specimens to be compacted, neither of the specimens were compacted to simulate 3DPC.

After placing the AAM in the cubes, the molds were covered with a plastic bag and stored in the laboratory at the ambient temperature of 23 ± 2o C for 12 hours and then cured at 50o C in an oven for another 12 hours (Kashosi et al. 2021). The compressive strength of the 3DPC specimens was determined in both parallel (X) and perpendicular (Z) directions (Figure 3). The reported results were the average of three specimens tested in each direction. The compressive strength was carried out for specimens having a CT of 1.0, 2.5, and 5.0 minutes for all mixtures. In addition, CT of 30 minutes and 60 minutes were carried out for mixtures 5 and 8. Moreover, while it may not be practical for 3DPC, CT of 24 hours was carried out for mixture 1 to investigate the effect of the very long CT on the strength of the test specimens.

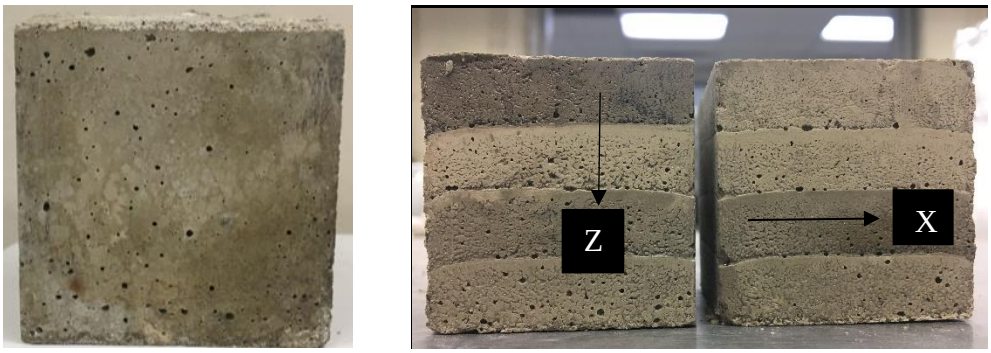

(a) (b)

Figure 3: (a) Full cube, and (b) Four layers of 3DPC specimens tested in Z and X directions.

2.4.2. Microstructural Analysis. Scanning electron microscopy (SEM) and energy-dispersive X-ray spectroscopy (EDS) were used to visualize and collect the elemental composition of the bond surface between two consecutive layers of the layered

mortar cubes. FEI Helios Naolab 600 DualBeam was used for the SEM scope. The images were acquired using the secondary electron (SE) detector. Test specimens, 10 x 10 x 50 mm, were cut from the cubes in a dry condition (Figure 4). The tested surface of each specimen was polished using 360, 800, and 1200 grit sandpapers, respectively. The specimens were dried by placing them at 40o C oven for 48 hours; then, the tested specimens were coated with gold before the SEM testing per ASTM C1723-16 procedure (ASTM-C1723 2016). Furthermore, elemental mapping was conducted to determine the elemental composition of the two layers at the bond surface.

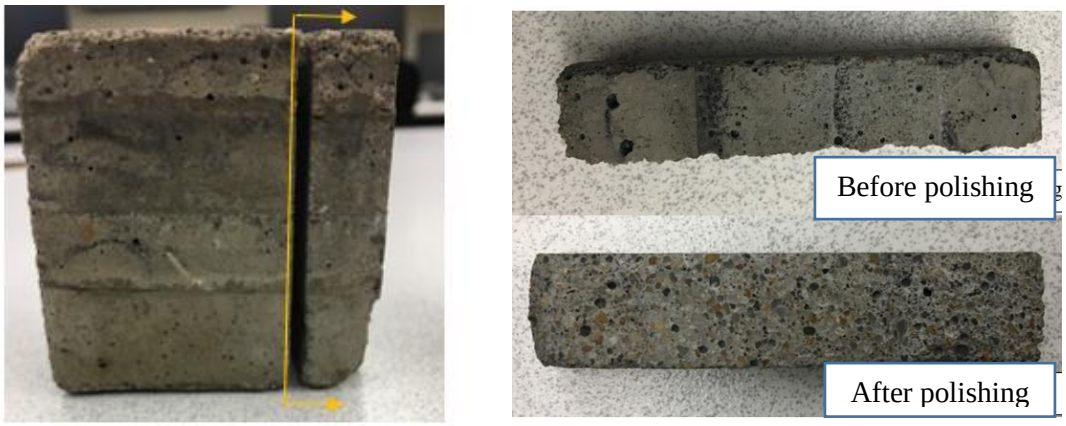

(a) (b)

Figure 4: Specimen's preparation for SEM testing: (a) cube after cutting the tested specimen and (b) tested specimen.

3. RESULTS AND DISCUSSION

In this section, the effect of the W/FA, Alk/FA, and SS/SH on the open time, deformability, and anisotropic compressive strength of AAM were discussed.

3.1. OPEN TIME

Figure 5a shows the effect of W/FA, Alk/FA, and SS/SH on the open time. As expected, the open time increased with increasing W/FA. When the W/FA ratio varies from 0.34 to 0.40 the open time increased from 2.5 minutes to 7.0 minutes but as the W/FA ratio increased beyond 0.42, the open time increased significantly to 31 minutes. Increasing the W/FA ratio increased the open time where the mixture will take longer time to lose its workability since W/FA had no role in the geopolymerization (Aliabdo et al. 2016) and subsequently decrease the concentration of the chemicals (i.e. SS and SH) (Gomaa et al. 2017).

Figure 5b shows the effect of Alk/FA for mixtures having W/FA of 0.36 and SS/SH of 1.0 on the open time. The open time decreased with increasing Alk/FA. Increasing the Alk/FA from 0.250 to 0.300 decreased the open time from 5.5 to 4.5 minutes. Alk/FA has a significant role in the geopolymerization reaction and it takes part in the dissolution of aluminosilicate geopolymers, low Alk/FA (i.e. SS and SH) may not be sufficient to dissolve the FA causing long open time, while high Alk/FA increases the dissolution rate of FA resulting in lower workability of the AAM and subsequently short open time (Gomaa et al. 2017; Siyal et al. 2016). In other words, increasing Alk/FA increases the soluble silica (SiO_2) and alkali (Na_2O) content in the mixture which accelerates the geopolymerization reaction, resulting in decreasing the time required to complete the dissolution process (Chindaprasirt et al. 2012; Siyal et al. 2016). Furthermore, SH has less viscosity than SS which resulted in higher workability (Provis and Bernal 2014) and longer open time.

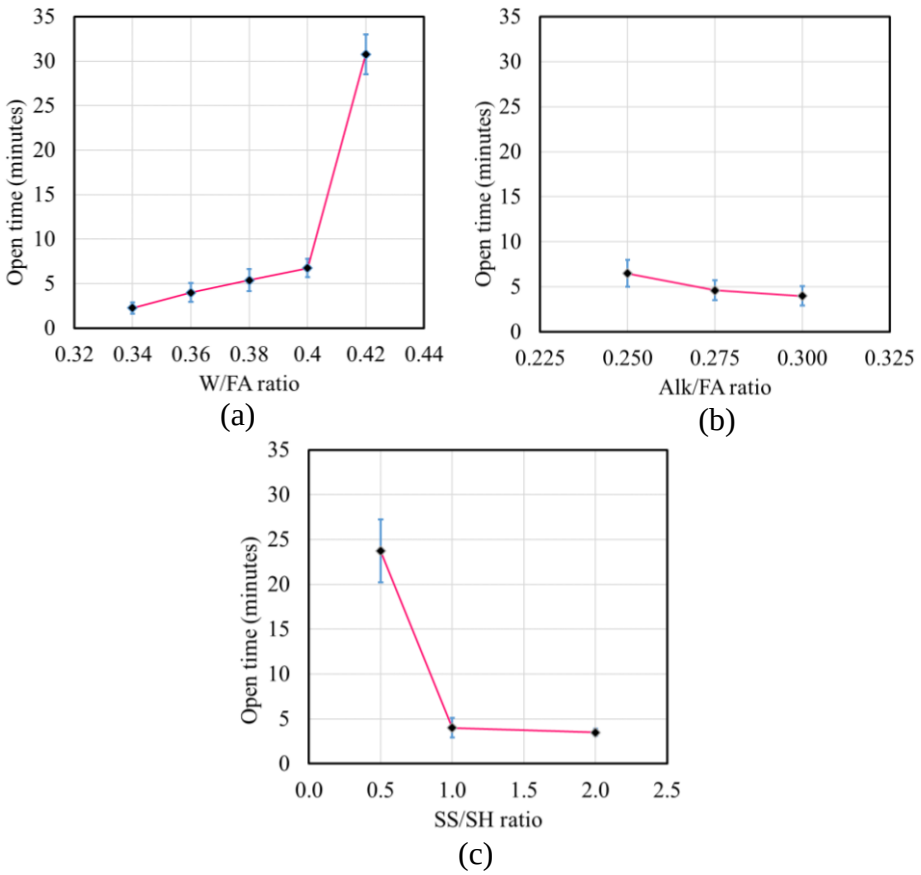

Figure 5: Effect of (a) W/FA ratio with Alk/FA of 0.300 and SS/SH of 1.0, (b) Alk/FA with W/FA of 0.36 and SS/SH of 1.0, and (c) SS/SH with W/FA of 0.36 and Alk/FA of 0.300 on the open time and setting time (Note: the difference in the vertical axis).

Figure 5c shows the effect of SS/SH for mixtures having W/FA of 0.36 and Alk/FA of 0.300 on the open time. As the SS/SH ratios increased, the open time decreased. Increasing the SS/SH from 0.5 to 2.0 decreased the open time from 20 minutes to 2.5 minutes. Increasing the SS content in the mixture increased the soluble silica (SiO2) and alkali (Na2O) content in the mixture. Therefore, increasing the silica by adding more SS decreased the setting time as the geopolymerization reaction was enhanced. Moreover, more free silicate in the solution took less time to complete the dissolution reaction resulting in decreasing the workability (Chindaprasirt et al. 2012;

Siyal et al. 2016). Thus, the open time decreased. As a result, this caused rapid workability loss of the AAM with time.

These results showed a wide range of open times. This is useful for users so they can select an appropriate mixture depending on the target printing time. Mixtures having shorter open times (i.e. from 2.5 minutes to 7 minutes) could be used to print a small structure such as a column. On the converse, longer open times (i.e. above 20 minutes) could be used to print a large structure such as a house. These varied open times provide the industry flexibility to determine which open time they need based on the type of structure and application target.

3.2. DEFORMATION

The effect of different CT was investigated to balance between fresh and hardened properties to satisfy less deformation and a high bond between subsequent layers.

3.2.1. Effect of the CT. Figure 6 (a-c) shows the effect of W/FA, Alk/FA, and SS/SH on the strain with increments of stacked loads at different CT. As the CT increased from 1.0 to 5.0 minutes, the strain decreased. At the CT of 1.0 minute, 2.5 minutes, and 5.0 minutes, the strain ranged from 1.23 to 11.2 %, 0.63 to 6.2%, and 0.24 to 1.37%, respectively. The number of stacked loads, which represent the number of layers, ranged from 5 to 9 based on the mixtures where the mixtures that had relatively low W/FA, high Alk/FA, high SS/SH, and long CT needed less number of staked loads to show approximately a constant strain readings and vice versa. For mix 5 and 8 which had longer open times, a longer CT of 30 and 60 minutes was used. The same observation

was obtained as the short CT's mixtures, where with increasing the CT from 30 minutes to 60 minutes, the strain decreased. At the CT of 30 minutes and 60 minutes, the strain ranged from 0.65 to 1.02 % and from 0.53 to 0.78%, respectively. Moreover, the number of stacked loads ranged from 3 to 5 for both mixtures. In general, longer CT of the material (i.e. layer) decreased the strain. With increasing CTs, the rate of evaporating of the free water increased which increased the hardening rate of the surface of the layer and improved the overall material stiffness which in turn caused the material to change from fluidity status to a plastic status so it can hold itself and other subsequent layers (Sanjayan et al. 2018; Zhang et al. 2018). These results were within the range of what was found in other studies where the strain of 3DPC based OPC for CT ranged from 18 seconds to 22 seconds (Zhang et al. 2018), 11 seconds to 60 seconds (Perrot et al. 2016), 15 minutes to 45 minutes (Zhang et al. 2018), 0 minute to 19 minutes (Kazemian et al. 2017), and 10 minutes to 80 minutes (Ma et al. 2018) was approximately ranged from 12.0 to 76.0% (Zhang et al. 2018), 37.5 to 54.6% (Perrot et al. 2016), 3.0 to 17.7% (Zhang et al. 2018), 0.0 to 11.5% (Kazemian et al. 2017), and 0.6 to 2.8% (Ma et al. 2018), respectively.

3.2.2. Effect of W/FA, Alk/FA, and SS/SH Ratios. Figure 6a shows the effect of W/FA ranged from 0.34 to 0.40 with Alk/FA of 0.300 and SS/SH of 1.0 on the strain with increments of stacked loads for CT of 1.0 minute, 2.5 minutes, and 5.0 minutes. The results revealed that the strain increased with increasing W/FA and the number of stacked loads. For W/FA ranged from 0.34 to 0.40 with CT of 1.0 minute, the strain ranged from 1.4 to 7.8% even once the number of stacked loads reached 8 or 9. This trend was the same when CT changed to 2.5 minutes and 5.0 minutes. When W/FA ranged from 0.34 to

0.42 with CT of 2.5 minutes and 5.0 minutes, the strain ranged from 0.65 to 6.22% and from 0.17 to 1.37% with the number of stacked loads reached to 7 and 6, respectively. With increasing the W/FA, the strain increased because mixtures had higher free water content which increased the workability (Aliabdo et al. 2016), and subsequently layer will be deformed easily. It is worth noting that the mixture with W/FA of 0.42 wasn't included (Figure 6a), since it had high strain; it reached up to 11.2% only after the first load.

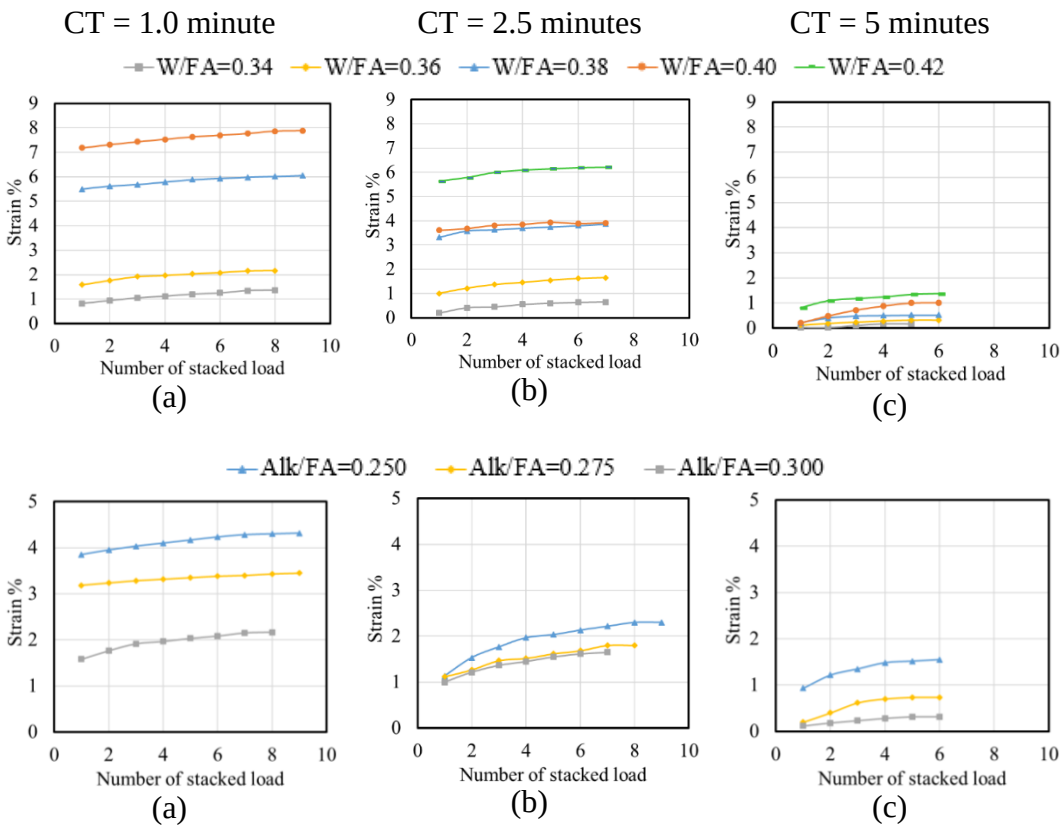

Figure 6: Effect of (a) W/FA ratio with Alk/FA of 0.300 and SS/SH of 1.0, (b) Alk/FA with W/FA of 0.36 and SS/SH of 1.0, and (c) SS/SH with W/FA of 0.36 and Alk/FA of 0.300 on the buildability in term of strain for a given number of stacked loads (Note: the vertical axis has different scale).

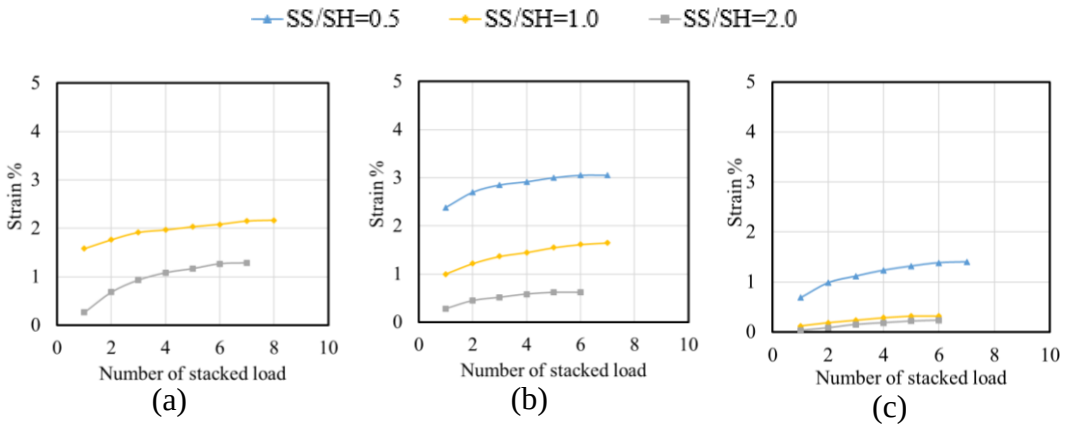

Figure 6: Effect of (a) W/FA ratio with Alk/FA of 0.300 and SS/SH of 1.0, (b) Alk/FA with W/FA of 0.36 and SS/SH of 1.0, and (c) SS/SH with W/FA of 0.36 and Alk/FA of 0.300 on the buildability in term of strain for a given number of stacked loads (Note: the vertical axis has different scale) (cont.).

Figure 6b shows the effect of Alk/FA ranged from 0.250 to 0.300 with W/FA of 0.36 and SS/SH of 1.0 on the strain with increments of stacked loads for CT of 1.0 minute, 2.5 minutes, and 5.0 minutes. The results revealed that the strain decreased with increasing Alk/FA. For Alk/FA ranged from 0.250 to 0.300 with CT of 1.0 minute, the strain ranged from 2.17 to 4.32% even once the number of stacked loads reached 8 or 9. This trend was the same when CT changed to 2.5 and 5.0 minutes. When Alk/FA ranged from 0.250 to 0.300 with CT of 2.5 and 5.0 minutes, the strain ranged from 1.65 to 2.30%, and from 0.33 to 1.55% with the number of stacked loads reached to 6. By increasing the Alk/FA, the gepolymeraization process is accelerated which results in lower setting time (i.e. workability) (Gomaa et al. 2017). This decreases the deformation which both enhances and improves the buildability.

Figure 6c shows the effect of SS/SH ranged from 0.5 to 2.0 with W/FA of 0.36 and Alk/FA of 1.0 on the strain with increments of stacked loads for CT of 1.0, 2.5, and 5.0 minutes. The results revealed that the strain decreased with increasing SS/SH. For

SS/SH ranged from 0.5 to 2.0 with CT of 1.0 minute, the strain ranged from 1.28 to 2.17% even once the number of stacked loads reached 7 or 9. This trend was the same when CT changed to 2.5 and 5.0 minutes. When SS/SH ranged from 0.5-2.0 with CT of 2.5 and 5.0 minutes, the strain ranged from 0.62 to 3.05% and from 0.23 to 1.40% with the number of stacked loads reached to 6. With increasing the SS/SH, the setting time was decelerated and the mixture lost its workability rapidly (Bondar et al. 2011) as explained previously which resulted in less deformation and good buildability. The mixture with a SS/SH of 0.5 wasn't included (Figure 6c) its high strain reached 10.1% after the first load.

3.3. COMPRESSIVE STRENGTH

In this section, the effect of the 3DPC, loading direction, and CT on the compressive strength is discussed as well as the effect of W/FA, Alk/FA, and SS/SH on compressive strength.

3.3.1. Effect of the 3DPC. Figure 7 shows the compressive strength results of the full and 3DPC specimens that had different CT. The compressive strength of the full specimens appeared to always be higher than those of 3DPC specimens. The compressive strengths of full specimens were 0.2 to 28% higher than 3DPC specimens tested in different directions (i.e. X and Z directions).

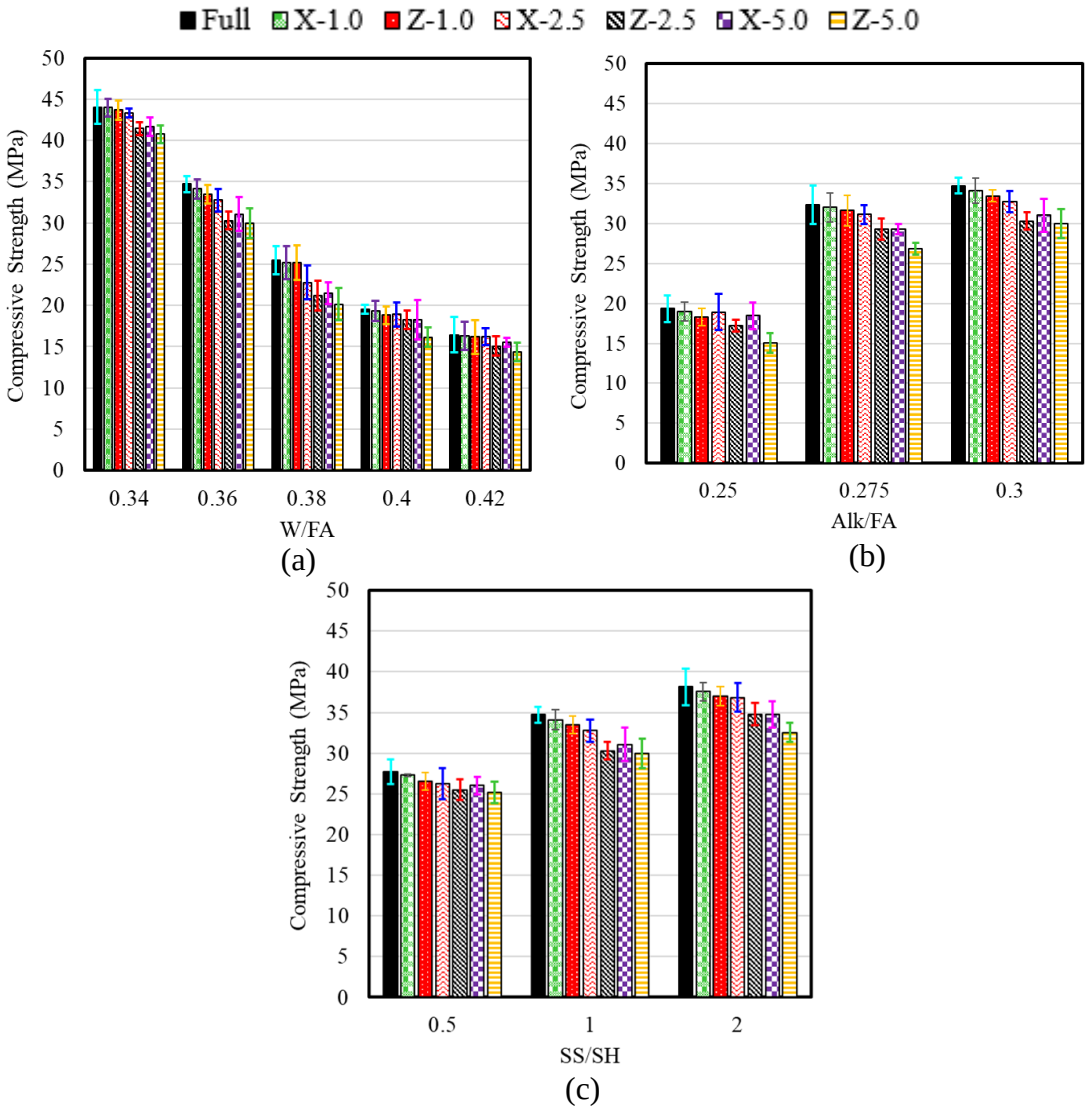

Figure 7: Effect of (a) W/FA ratio with Alk/FA of 0.300 and SS/SH of 1.0, (b) Alk/FA with W/FA of 0.36 and SS/SH of 1.0, and (c) SS/SH with W/FA of 0.36 and Alk/FA of 0.300 on the compressive strength of full and 3DPC specimens having different CT (Note: CT in minute in the legend).

These results were similar to what was reported for 3DPC specimens based OPC (Le et al. 2012; Rahul et al. 2019) where the reduction in compressive strengths of 3DPC specimens tested in all directions ranged from 12.8-19.6% (Rahul et al. 2019) and from 5 to 30% (Le et al. 2012) compared with full specimens. The decrease of the compressive strength for the 3DPC specimens compared with full-specimens can be explained by

three reasons. First, placing the consecutive layers of the 3DPC specimens without compaction cause relatively insufficient interaction and interlinkage between two layers compared with the full specimens which slightly weakened the bond between the layers and strength of 3DPC specimens (Tay et al. 2019). Second, placing the consecutive layers of the 3DPC without compaction trapped air voids between the layers and subsequently increased the voids content of the 3DPC specimens compared with those of full specimens which could be seen by the higher porosity of the 3DPC specimens compared with the full specimens (Le et al. 2012; Rahul et al. 2019). Third, in the 3DPC specimens, there was a moisture loss from the top surface of each layer which subsequently negatively affected the bond between the consecutive layers and decreased the compressive strength compared with those of full specimens (Sanjayan et al. 2018).

3.3.2. Effect of the Loading Direction. Figure 7 shows the compressive strength results of the full and 3DPC specimens tested in X and Z directions for different ratios of W/FA, Alk/FA, and SS/SH. It was observed that the compressive strength of 3DPC specimens depends on the testing direction where the compressive strengths of the tested specimens in the X-direction were always higher than those of the Z-direction. The compressive strength in X-direction were higher by 0.03 to 3.5%, 3.6 to 10%, 2.2 to 22.7%, 4.6 to 10.3%, and 7.1 to 13.5% than those of Z-direction for the 3DPC specimens had a CT of 1.0, 2.5, 5.0, 30, and 60 minutes, respectively (Figure 7).

The compressive strength results showed anisotropic phenomena (i.e. compressive strength was different in X-direction as compared with Z-direction) for 3DPC specimens tested in different directions which were in line with what was found in another study. It was found that the compressive strength of 3DPC specimens based OPC

tested in X-direction was higher by 10 to 21.7% than those specimens tested in. Z-direction (Paul et al. 2018). The explanation for this is that a higher compressive strength in X-direction compared with Z-direction is associated with shear-induced by platen friction exploiting any flaws at the bead boundaries (Le et al. 2012). In other words, when specimens are tested in the Z-direction, the load beds begin to separate, while when testing in the X-direction the load is distributed uniformly result in higher strengths (Panda et al. 2017). The X-direction also showed the highest compressive strength due to the increased density in this direction caused by pressure exerted during mortar placing which resulted in higher packing of the material (Panda et al. 2017). Moreover, the surface quality also affected the results of the tested 3DPC specimens in Z-direction, where the tested specimens in Z-direction were exposed to stress on the upper surface that was not perfectly flat and had some imperfections compared to those specimens tested in X-direction that was exposed to stress on the sides of the cubes that were perfectly flat.

3.3.3. Effect of the CT. Figure 7 shows the compressive strength results of the full and 3DPC specimens having different CT. When the CT increased, the compressive strength decreased. For a CT of 1.0 minute, the compressive strength for 3DPC specimens tested in both directions was very close to the full specimens. The reduction in the compressive strength of 3DPC specimens tested in both directions ranged from 0.21 to 5.3% compared with full specimens. While for CT of 2.5 minutes and 5.0 minutes, the reduction ranged from 1.3 to 16.6% and from 4.7 to 20.9% compared with full specimens, respectively. In addition, the compressive strength was carried out on 3DPC specimens having long CT of 30 minutes and 60 minutes for mixtures 5 and 8 since they

had relatively long open time, thus the reduction ranged from 6.6 to 19.7% and from 7.3 to 22.1%, respectively. The failure pattern was very close to the full molds for CTs ranged from 1 to 60 minutes (Figure8a-b) which explained the relatively low reduction in the strength of the 3DPC specimens compared with those of full specimens.

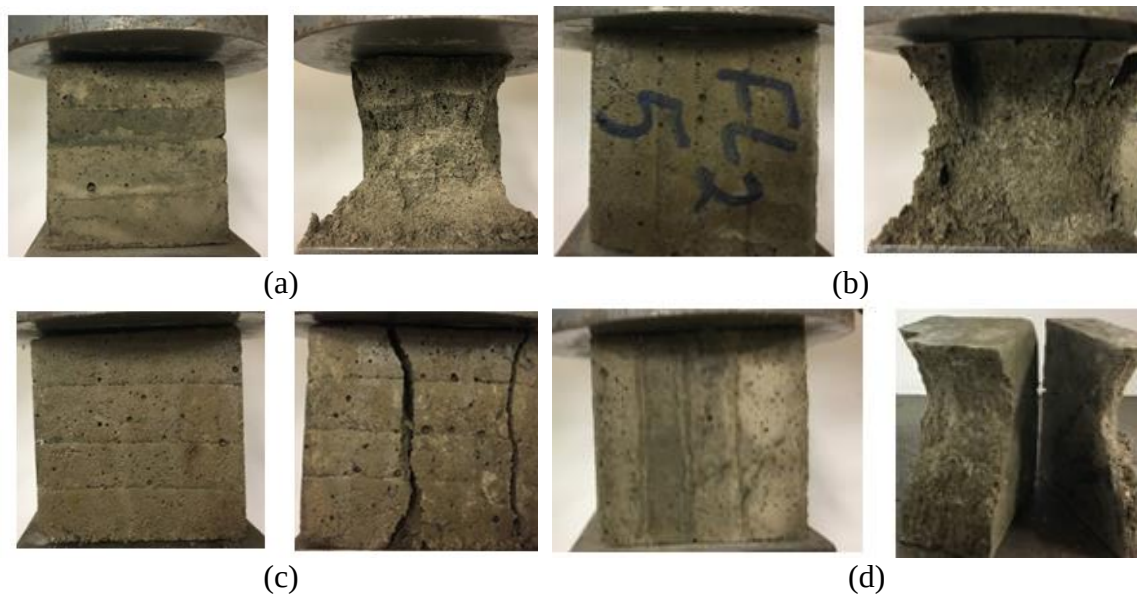

(a) (b)

(c) (d)

Figure 8: Failure patterns in compression test for 3DPC specimens tested in: (a) Z-direction, (b) X-direction with CT of 5.0 minutes, (c) Z-direction, and (d) X-direction with CT of 24 hours.

Compressive strength was carried out for mixture1 with CT of 24 hours to investigate the effect of the very long of CT on the bond strength. It was found that the reduction of the compressive strength reached 51% compared with full specimens. However, as shown in (Figure 8c-d), the failure patterns were normal due to the shear effect from two ends. The explanation for the reduction in the compressive strength of the 3DPC specimens with increasing CT is twofold. First, the loss of the moisture content (i.e. evaporation rate) of the surface of the layer increases with increasing the CT which affects the bond between the subsequent layers negatively. Second, with increasing CT,

there is additional time for FA particle nucleation to occur which increases the hardening rate of the surface of the layer and improves the material's stiffness. This increase in stiffness causes less disruption on the interfacial material as CT increases and subsequently causes lower bond strength between the consecutive layers due to the insufficient interaction between layers (Tay et al. 2019).

3.3.4. Effect of the W/FA, Alk/FA, and SS/SH Ratios. Figure 7a shows the effect of W/FA on the compressive strength for the full and the 3DPC in different directions with fixed Alk/FA and SS/SH of 0.300 and 1.0, respectively. With increasing W/FA the compressive strength of both full and 3DPC specimens decreased. When W/FA ranged from 0.34-0.42 of both full and 3DPC specimens, the compressive strengths ranged from 44.1 to 14.3 MPa. This reduction in compressive strength is potentially due to the increased W/FA, which increased the formation of voids increased since the water had no role in the geopolymeraization reaction, resulted in lower compressive strength (Aliabdo et al. 2016).

Figure 7b shows the effect of Alk/FA on the compressive strength for the full and the 3DPC in different directions with fixed W/FA and SS/SH of 0.36 and 1.0, respectively. With increasing Alk/FA, the compressive strength of both full and 3DPC specimens decreased. When Alk/FA ranged from 0.250 to 0.300 of both full and 3DPC specimens, the compressive strengths ranged from 15.0 to 34.7 MPa. This trend could be due to the increasing the alkali activator (i.e. SS and SH) which increased both the silica and alumina solubility and the Na_2O which resulted in a higher rate of geopolymarization and higher compressive strength (Gomaa et al. 2017).

Figure 7c shows the effect of SS/SH on the compressive strength for the full and the 3DPC in different directions with fixed W/FA and Alk/FA of 0.36 and 0.300, respectively. With increasing SS/SH the compressive strength of both full and 3DPC specimens increased. When Alk/FA ranged from 0.5 to 2.0 of both full and 3DPC specimens, the compressive strengths ranged from 22.6 to 38.2 MPa. Generally, increasing SS/SH ratio enhances the geopolymaraization process as a result the compressive strength increased (Gomaa et al. 2017). With increasing SS/SH ratio, more soluble silica (SiO2) increased in the mortar which increased the SiO2/Al2O3 ratio resulted in more Si-O-Si bond and higher compressive strength (Aliabdo et al. 2016; Bong et al. 2018; Gomaa et al. 2017).

3.3.5. Microstructural Analysis of the Bond Area. The SEM images and line scan of the 3DPC specimens of M1 having CT of 2.5 minutes and 24 hours are shown in Figure 9 and Figure 10, respectively. Those two specimens having two CTs were selected to explain the strong and relatively weak bond "compressive strength" between the layers having short and long CT, respectively. The SEM images show the top layer, bottom layer, and bond area between the two layers. Different elements such as Si, Ca, Al, Na, and Mg were distributed in the elemental line scan of the specimen based on the existed components as the following (Figure 10a and b). 1) Areas that had a high intensity of Si were detected as sand particles (Noted as "S"). 2) Areas that had a high intensity of Si, Al, and Na were detected as the aluminosilicate gel (N-A-S-H) (Noted as "N"). 3) Areas that had a high intensity of Si, Al, Na, and Ca were detected as aluminosilicate gel with calcium (C-N-A-S-H) (Noted as "C"). 4) Black areas were detected as voids.

For the specimen having a CT of 2.5 minutes, the different elements were distributed approximately evenly in the top layer, bottom layer, and bond area (Figure 10a). The bond area was not obvious in the SEM image (Figure 9a) and it was homogeneously blended with the top and bottom layers (Figure10a). (Note: the bond area of this specimen was determined and marked before SEM testing as shown in Figure 4) Moreover, there were no voids existed in the bond area. Therefore, relatively high compressive strengths were obtained for 3DPC specimens having short CT (Figure 7).

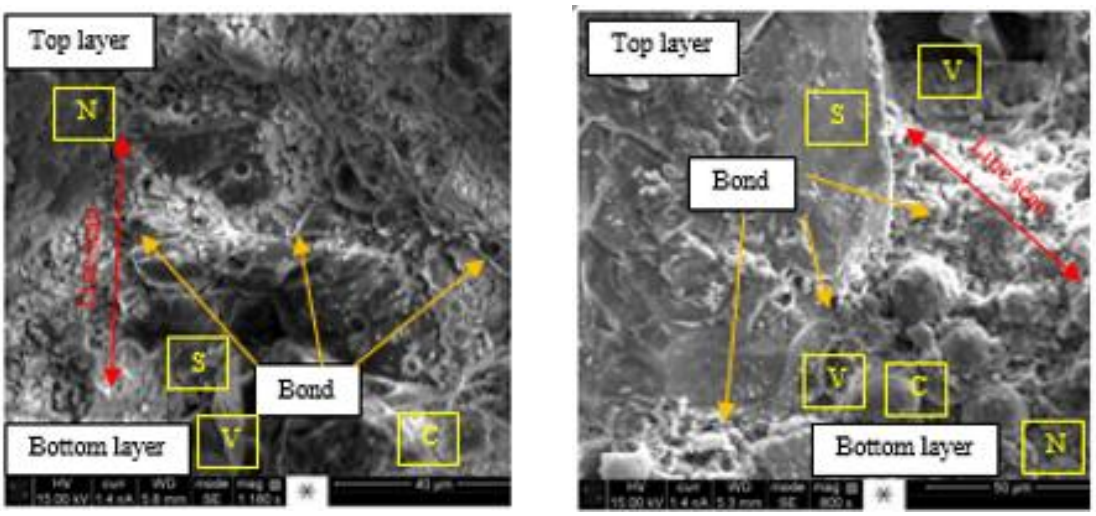

(a) (b)

Figure 9: SEM images of M1 with CT of (a) 2.5 minutes, and (b) 24 hours of the 3DPC.

For the specimen having CT of 24 hours, the different elements were distributed approximately evenly in the top and bottom layers (Figure 10b). Although the SEM did not show a clear separation line between the top and bottom layers at the bond area (Figure9a), However, there was a drop in the intensity of the different elements at the bond area between the top and bottom layers (Figure 10b). That drop was due to the relatively long CT (i.e. 24 hours) that affected the interconnection between the top and

bottom layers negatively. Moreover, there were voids “entrapped air voids” between the top and bottom layers at the bond area (Figure 10b). This explains the roughly 50% decrease in the compressive strength of the 3DPC specimen with CT of 24 hours compared to a full specimen.

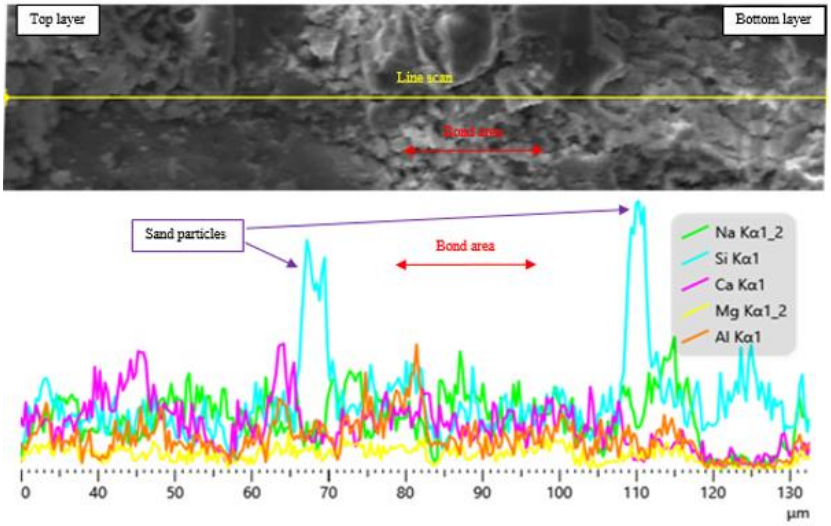

(a)

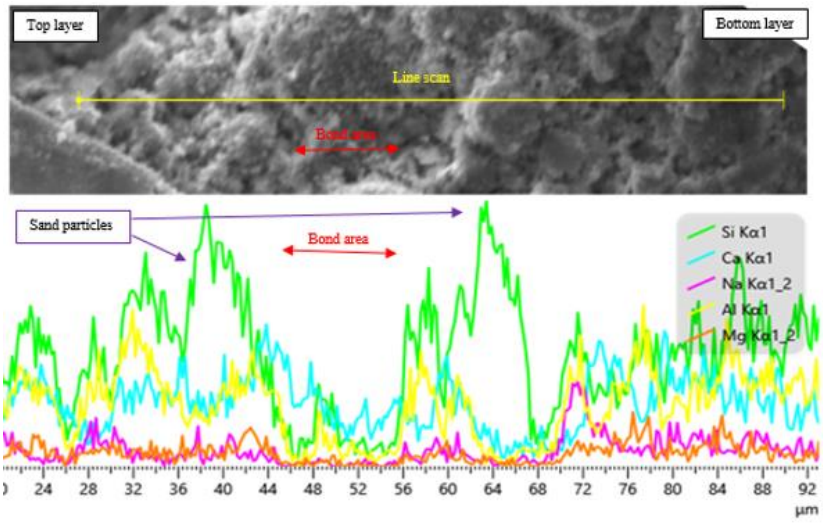

(b)

Figure 10: Elemental line scan of M1 with CT of: (a) 2.5 minutes, and (b) 24 hours.

4. PROVIDING WIDE RANGE OF MIXTURES FOR DIFFERENT APPLICATIONS

Based on all 3DPC properties that were studied, 3DPC based AAM offered a wide range of selections of open time, deformations, and cycle time without adding any admixtures such as accelerators, retarders, or superplasticizer. The open time was extended from 3.5 to 24 minutes by decreasing the SS/SH from 2.0 to 0.5 with fixed W/FA and Alk/FA of 0.36 and 0.300, respectively. Moreover, to obtain an open time range from 4 to 7 minutes, different mix designs could be used such as a mixture which consists of W/FA, Alk/FA, and SS/SH of 0.38, 0.300, and 1.0, respectively, or decreasing both W/FA and Al/k/FA to 0.36 and 0.275, respectively.

In terms of the acceptable deformations, specified strain limits can be satisfied in different ways. For example, a strain limit of 2% can be maintained through the following: first, for mixtures 1 and 2 which had W/FA of 0.34 and 0.36, respectively, with fixed Alk/FA and SS/SH of 0.300 and 1.0, the maximum strain was approximately 2% with all CTs. Second, with increasing the CT to 5.0 minutes, all mixtures had a maximum strain of 2%. Third, with decreasing the Alk/FA to 0.275 or 0.250 (i.e. mixtures 6 and 7, respectively), W/FA of 0.36, and SS/SH of 1.0, the maximum limited strain of 2 % was obtained with CT of 2.5 minutes and 5.0 minutes, respectively. Fourth, by increasing the SS/SH to 2.0 (i.e. mixture 9), the maximum limited strain of 2 % was obtained for all CTs. Fifth, with decreasing the SS/SH to 0.5 with W/FA of 0.36 and Alk/FA of 0.300 (i.e. mixture 8), with CT of 30 and 60 minutes, a maximum strain of 1 % was obtained. Thus, these wide options of the different ways to achieve a strain of 2 % provide the flexibility to the industry to select the mixture based on their target toward

3DPC with strain ranged from 0.17 to 2.10 %. Thus, it could be said that CT can range from 1 to 60 minutes.

In terms of compressive strength, regardless of the anisotropic phenomena for 3DPC specimens, all mixtures showed acceptable compressive strength ranging from 44.0 to 20.4 MPa for structural applications with all CTs except mixtures 4, 5, and 7 where their compressive strengths were low for both full and 3DPC specimens (i.e. ranged from 14.4 to 19.5 MPa). Table 3 shows the different mixtures had different mix designs, open time, and CT that were accepted in terms of deformation and compressive strength.

Table 3: Results of the accepted mixtures.

Mixture no.	W/FA	Alk/FA	SS/SH	Open time (min)	CT (min)	Strain (%)	fc' X-direction (MPa)	fc' Z-direction (MPa)
1	0.34	0.300	1.0	2.5	1.0	1.40	44.0	43.7
1	0.34	0.300	1.0	2.5	2.5	0.65	43.3	41.4
1	0.34	0.300	1.0	2.5	5.0	0.17	41.7	40.8
2	0.36	0.300	1.0	4	1.0	2.10	34.1	33.5
2	0.36	0.300	1.0	4	2.5	1.65	32.8	30.3
2	0.36	0.300	1.0	4	5.0	0.32	31.1	30.0
3	0.38	0.300	1.0	5.5	5.0	0.52	22.8	20.4
6	0.36	0.275	1.0	5	2.5	1.80	31.2	29.3
6	0.36	0.275	1.0	5	5.0	0.73	29.3	26.9
8	0.36	0.300	0.5	24	30.0	0.65	25.9	24.8
8	0.36	0.300	0.5	24	60.0	0.53	25.7	22.6
9	0.36	0.300	2.0	3.5	1.0	1.28	37.6	37.0
9	0.36	0.300	2.0	3.5	2.5	0.62	36.9	34.8
9	0.36	0.300	2.0	3.5	5.0	0.23	34.8	32.6

5. CONCLUSION

In this study, the applicability of using class C FA for 3DPC was investigated in order to offer wide options of mixtures that can be used in various 3D printing applications. The fresh properties (i.e. extrudability and buildability in terms of open time and deformation) and compressive strength were investigated through studying the effect of W/FA, Alk/FA, and SS/SH on these properties. In addition, the effect of the CT on the deformation and compressive strength of 3DPC specimens tested in two directions was investigated. Based on the results, the following conclusions were made:

- A wide range in open time was achieved by controlling the W/FA, Alk/FA, and SS/SH. The open time, during which materials could be extruded, ranged from 2.5 to 31.0 minutes.
- Increasing the CT between loads decreased the deformation since the material gained enough strength to resist the deformation. The CT ranged from 1.0 to 60.0 minutes to limit the maximum accepted strain to 2%. However, a wider range of CT can be used with higher strain limits.
- Increasing W/FA resulted in higher deformation while increasing the Alk/FA and SS/SH resulted in lower deformation. The strain ranged from 0.17 to 11.2 % with different W/FA, Alk/FA, and SS/SH ratios.
- The compressive strength of full specimens was higher by 0.2 to 28.0 % than 3DPC specimens tested in both directions.
- The results showed an anisotropic phenomenon of 3DPC specimens. In other words, the compressive strength was dependent on the test direction (i.e. X or Z direction).

The compressive strength of 3DPC specimens tested in the X-direction was higher by 0.03 to 22.7 % than 3DPC tested in Z-direction.

- By applying a longer CT, the compressive strength of 3DPC specimens was decreased in both directions tested due to the lower bond strength between layers. The reduction in the compressive strength reached 51 % with a CT of 24 hours compared with 1.0 minutes.
- A 3DPC based class C FA was successfully developed with a wide range of options to meet the construction industry requirement allowing for the flexibility in printing different shapes and their target strength in different directions. These results allow the industry to select which mix design fits their needs and target for 3DPC based on the type of structure.
- The SEM images and the line scan analyses showed an even distribution in the intensity of the different elements in the top layer, bottom layer, and bond area of 3DPC specimen having short CT which explains its relatively high compressive strength. However, a drop in the intensity of the different elements and voids at the bond area of the 3DPC specimen having long CT which explains its relatively low compressive strength.

6. RECOMMENDATION

This study mainly focused on investigating the applicability of using class C FA based geopolymer mortar in simulating 3D printing. Future work can be focused on rheological properties of class C FA based geopolymer mortar and measuring the

shear deformation since this study primarily focused on measuring normal deformation. In addition, tensile strength can be carried further investigated in order to better out best understand the bond strength.

REFERENCES

Alghamdi, H., Nair, S. A., and Neithalath, N. (2019). "Insights into material design, extrusion rheology, and properties of 3D-printable alkali-activated fly ash-based binders." *Materials & Design*, 167, 107634.

Aliabdo, A. A., Abd Elmoaty, M., and Salem, H. A. (2016). "Effect of water addition, plasticizer and alkaline solution constitution on fly ash based geopolymer concrete performance." *Construction and Building Materials*, 121, 694-703.

ASTM-C109/C109M (2016). "Standard test method for compressive strength of hydraulic cement mortars (using 2-in. or [50-mm] cube specimens)." *ASTM International*.

ASTM-C230/230M (2008). "Standard Specification for Flow Table for Use in Tests of Hydraulic Cement." *ASTM International*.

ASTM-C618 (2015). "Standard Specification for Coal Fly Ash and Raw or Calcined Natural Pozzolan for use in Concrete." *ASTM International*.

ASTM-C1437 (2015). "Standard Test Method for Flow of Hydraulic Cement Mortar." *ASTM International*.

ASTM-C1723 (2016). "Standard guide for examination of hardened concrete using scanning electron microscopy." *ASTM International*.

Bondar, D., Lynsdale, C., Milestone, N. B., Hassani, N., and Ramezanianpour, A. (2011). "Effect of type, form, and dosage of activators on strength of alkali-activated natural pozzolans." *Cement and Concrete Composites*, 33(2), 251-260.

Bong, S. H., Nematollahi, B., Nazari, A., Xia, M., and Sanjayan, J. G. "Fresh and hardened properties of 3D printable geopolymer cured in ambient temperature." *Proc., RILEM International Conference on Concrete and Digital Fabrication*, Springer, 3-11.

Chindaprasirt, P., De Silva, P., Sagoe-Crentsil, K., and Hanjitsuwan, S. (2012). "Effect of SiO 2 and Al 2 O 3 on the setting and hardening of high calcium fly ash-based geopolymer systems." *Journal of Materials Science*, 47(12), 4876-4883.

Duxson, P., and Provis, J. L. (2008). "Designing precursors for geopolymer cements." *Journal of the American Ceramic Society*, 91(12), 3864-3869.

Feng, P., Meng, X., Chen, J.-F., and Ye, L. (2015). "Mechanical properties of structures 3D printed with cementitious powders." *Construction and Building Materials*, 93, 486-497.

Gao, W., Zhang, Y., Ramanujan, D., Ramani, K., Chen, Y., Williams, C. B., Wang, C. C., Shin, Y. C., Zhang, S., and Zavattieri, P. D. (2015). "The status, challenges, and future of additive manufacturing in engineering." *Computer-Aided Design*, 69, 65-89.

Gomaa, E., Han, T., ElGawady, M., Huang, J., and Kumar, A. (2021). "Machine learning to predict properties of fresh and hardened alkali-activated concrete." *Cement and Concrete Composites*, 115, 103863.

Gomaa, E., Sargon, S., Gheni, A., and ElGawady, M. "Mechanical properties of alkali activated concrete based class C fly ash." *Proc., 9th International Conference on Bridge Maintenance, Safety and Management (IABMAS 2018)*.

Gomaa, E., Sargon, S., Kashosi, C., and ElGawady, M. (2017). "Fresh properties and compressive strength of high calcium alkali activated fly ash mortar." *Journal of King Saud University-Engineering Sciences*, 29(4), 356-364.

Gomaa, E., Sargon, S., Kashosi, C., and ElGawady, M. "Fresh properties and early compressive strength of alkali-activated high calcium fly ash paste." *Proc., Congrès International de Géotechnique–Ouvrages–Structures*, Springer, 497-507.

Gomaa, E., Sargon, S., Kashosi, C., Gheni, A., and ElGawady, M. A. (2020). "Mechanical Properties of High Early Strength Class C Fly Ash-Based Alkali Activated Concrete." *Transportation Research Record*, 0361198120915892.

Gomaa, E. Y., Gheni, A. A., and ElGawady, M. A. (2019). "Durability of Class C Fly Ash-Based Alkali Activated Concrete." *ACI Special Publication*, 334, 185-204.

Hager, I., Golonka, A., and Putanowicz, R. (2016). "3D printing of buildings and building components as the future of sustainable construction?" *Procedia Engineering*, 151, 292-299.

Jha, K. N. (2012). *Formwork for concrete structures*, Tata McGraw Hill Education Private Limited.

Kashani, A., and Ngo, T. "Optimisation of mixture properties for 3D printing of geopolymer concrete." *Proc., ISARC. Proceedings of the International Symposium on Automation and Robotics in Construction*, IAARC Publications, 1-8.

Kashosi, C., Gheni, A., Gomaa, E., and ElGawady, M. (2021). "Effects of Rest Time and Curing Regime on Short and Long-Term Strength of Class C Fly Ash-Based Alkali Activated Mortars."

Kazemian, A., Yuan, X., Cochran, E., and Khoshnevis, B. (2017). "Cementitious materials for construction-scale 3D printing: Laboratory testing of fresh printing mixture." *Construction and Building Materials*, 145, 639-647.

Le, T. T., Austin, S. A., Lim, S., Buswell, R. A., Gibb, A. G., and Thorpe, T. (2012). "Mix design and fresh properties for high-performance printing concrete." *Materials and structures*, 45(8), 1221-1232.

Le, T. T., Austin, S. A., Lim, S., Buswell, R. A., Law, R., Gibb, A. G., and Thorpe, T. (2012). "Hardened properties of high-performance printing concrete." *Cement and Concrete Research*, 42(3), 558-566.

Li, Z., Wang, L., and Ma, G. (2018). "Method for the enhancement of buildability and bending resistance of 3D printable tailing mortar." *International Journal of Concrete Structures and Materials*, 12(1), 37.

Ma, G., Li, Z., and Wang, L. (2018). "Printable properties of cementitious material containing copper tailings for extrusion based 3D printing." *Construction and building materials*, 162, 613-627.

Ma, G., Wang, L., and Ju, Y. (2018). "State-of-the-art of 3D printing technology of cementitious material—An emerging technique for construction." *Science China Technological Sciences*, 61(4), 475-495.

Malaeb, Z., Hachem, H., Tourbah, A., Maalouf, T., El Zarwi, N., and Hamzeh, F. (2015). "3D concrete printing: machine and mix design." *International Journal of Civil Engineering*, 6(6), 14-22.

Marchment, T., Xia, M., Dodd, E., Sanjayan, J., and Nematollahi, B. "Effect of delay time on the mechanical properties of extrusion-based 3D printed concrete." *Proc., Proceedings of the International Symposium on Automation and Robotics in Construction, Taipei, Taiwan*.

Mechtcherine, V., Nerella, V. N., and Kasten, K. (2014). "Testing pumpability of concrete using Sliding Pipe Rheometer." *Construction and Building Materials*, 53, 312-323.

Nematollahi, B., Vijay, P., Sanjayan, J., Nazari, A., Xia, M., Naidu Nerella, V., and Mechtcherine, V. (2018). "Effect of Polypropylene Fibre Addition on Properties of Geopolymers Made by 3D Printing for Digital Construction." *Materials*, 11(12), 2352.

Nerella, V. N., and Mechtcherine, V. (2019). "Studying the Printability of Fresh Concrete for Formwork-Free Concrete Onsite 3D Printing Technology (CONPrint3D)." *3D Concrete Printing Technology*, Elsevier, 333-347.

Ngo, T. D., Kashani, A., Imbalzano, G., Nguyen, K. T., and Hui, D. (2018). "Additive manufacturing (3D printing): A review of materials, methods, applications and challenges." *Composites Part B: Engineering*, 143, 172-196.

Panda, B., Paul, S. C., Hui, L. J., Tay, Y. W. D., and Tan, M. J. (2017). "Additive manufacturing of geopolymer for sustainable built environment." *Journal of cleaner production*, 167, 281-288.

Panda, B., Paul, S. C., Mohamed, N. A. N., Tay, Y. W. D., and Tan, M. J. (2018). "Measurement of tensile bond strength of 3D printed geopolymer mortar." *Measurement*, 113, 108-116.

Panda, B., Paul, S. C., and Tan, M. J. (2017). "Anisotropic mechanical performance of 3D printed fiber reinforced sustainable construction material." *Materials Letters*, 209, 146-149.

Panda, B., and Tan, M. J. (2018). "Experimental study on mix proportion and fresh properties of fly ash based geopolymer for 3D concrete printing." *Ceramics International*, 44(9), 10258-10265.

Panda, B., Unluer, C., and Tan, M. J. (2018). "Investigation of the rheology and strength of geopolymer mixtures for extrusion-based 3D printing." *Cement and Concrete Composites*, 94, 307-314.

Papachristoforou, M., Mitsopoulos, V., and Stefanidou, M. (2018). "Evaluation of workability parameters in 3D printing concrete." *Procedia Structural Integrity*, 10, 155-162.

Paul, S. C., Tay, Y. W. D., Panda, B., and Tan, M. J. (2018). "Fresh and hardened properties of 3D printable cementitious materials for building and construction." *Archives of civil and mechanical engineering*, 18(1), 311-319.

Perrot, A., Rangeard, D., and Pierre, A. (2016). "Structural built-up of cement-based materials used for 3D-printing extrusion techniques." *Materials and Structures*, 49(4), 1213-1220.

Provis, J. L., and Bernal, S. A. (2014). "Geopolymers and related alkali-activated materials." *Annual Review of Materials Research*, 44, 299-327.

Rahul, A., Santhanam, M., Meena, H., and Ghani, Z. (2019). "Mechanical characterization of 3D printable concrete." *Construction and Building Materials*, 227, 116710.

Sanjayan, J. (2016). "Materials technology research to structural design of geopolymer concrete." *Mechanics of Structures and Materials XXIV*, CRC Press, 60-69.

Sanjayan, J. G., Nematollahi, B., Xia, M., and Marchment, T. (2018). "Effect of surface moisture on inter-layer strength of 3D printed concrete." *Construction and Building Materials*, 172, 468-475.

Siyal, A. A., Azizli, K. A., Man, Z., and Ullah, H. (2016). "Effects of parameters on the setting time of fly ash based geopolymers using Taguchi method." *Procedia engineering*, 148, 302-307.

Sumer, M. (2012). "Compressive strength and sulfate resistance properties of concretes containing Class F and Class C fly ashes." *Construction and Building Materials*, 34, 531-536.

Tay, Y. W. D., Ting, G. H. A., Qian, Y., Panda, B., He, L., and Tan, M. J. (2019). "Time gap effect on bond strength of 3D-printed concrete." *Virtual and Physical Prototyping*, 14(1), 104-113.

Wolfs, R., Bos, F., and Salet, T. (2019). "Hardened properties of 3D printed concrete: The influence of process parameters on interlayer adhesion." *Cement and Concrete Research*, 119, 132-140.

Xia, M., Nematollahi, B., and Sanjayan, J. (2019). "Printability, accuracy and strength of geopolymer made using powder-based 3D printing for construction applications." *Automation in Construction*, 101, 179-189.

Yacob, N. S., ElGawady, M. A., Sneed, L. H., and Said, A. (2019). "Shear strength of fly ash-based geopolymer reinforced concrete beams." *Engineering Structures*, 196, 109298.

Zhang, Y., Zhang, Y., Liu, G., Yang, Y., Wu, M., and Pang, B. (2018). "Fresh properties of a novel 3D printing concrete ink." *Construction and building materials*, 174, 263-271.

II. NUMERICAL ANALYSIS OF LAYERED CONCRETE ENCASING CORRODED STEEL BRIDGE COLUMN

ABSTRACT

This study numerically investigates corroded steel H-piles repaired using concrete encasement subjected to axial loads. Five FE models were developed using LS-DYNA software of severely corroded full-scale steel H-pile repaired using the concrete encasement method. Two types of concrete encasement were studied, full encasement and layered encasement to mimic 3D printed concrete. First, the model was validated against the experimental results of the tested steel H-pile model severely corroded under axial compression. Then, the developed models were implemented to conduct a parametric study investigating the effect of the concrete encasement type in terms of the failure modes, obtained axial capacity, and coefficient of friction between the layered. The numerical results showed that increasing the coefficient of friction by 14.0% increased the axial capacity of the repaired specimens by 11.3% compared to the virgin steel H-pile. However, in general, the failure mode of the specimens was the same. Debonding phenomena were observed regardless of the coefficient of friction between the layered concrete.

1. INTRODUCTION

Steel H-piles are widely used in bridge construction throughout the U.S. due to their relatively large load carrying capacity while simultaneously occupying a small area. Unfortunately, many H-piles suffer from various corrosion levels due to their exposure to the environmental conditions (i.e., repeated wetting and drying cycles) throughout their service life. This subsequently impairs their structural integrity, capacity, and serviceability and can lead to abrupt collapse (Iskander and Stachula 2002; Karagah et al. 2015; Shi et al. 2014). In many cases, the total replacement is not an option due to the high cost. Therefore, new techniques with long-lasting durability and require less maintenance during the bridge's extended service life need to be developed and investigated since more than 37% of US bridges need repair work (Rahul et al. 2019).

Several methods for repairing the steel piles have been used by many US DOTs (Abdulazeez et al. 2019; Dawood et al. 2017; Wipf et al. 2003) to strengthen and restore the original axial carrying capacity of corroded piles. Such methods include using a confined concrete jacket (Ehsani 2009; Karagah et al. 2018; Liu et al. 2001) or adding steel plates (Wan et al. 2013). Out of these utilized repair methods, the concrete jacket was found to be simple to implement, in which the corroded portion of the steel pile was encased fully in a concrete jacket (Abdulazeez et al. 2019). The concrete jacket repair method can serve as an alternative load path for the applied axial load by confining the damaged region and increasing its effective stiffness, thus reducing the risk of the bridge collapse.

A potential approach to repair corroded H pile steel is by using 3D printed concrete encasement. 3D printing, often referred to as additive manufacturing, is the new technology that can build a complex structure by depositing concrete layer by layer without formwork (Ngo et al. 2018). It has many advantages compared with conventional concrete (CC), including; reduce materials waste, cutting time and workmanship, and subsequently reducing the cost (Ma et al. 2018). Thus, it could be used to print the layered concrete as a jacket around the corroded steel H-pile.

Different types of concrete jacket could be used to repair the corroded steel H-pile, including conventional concrete and geopolymer concrete. Geopolymer concrete, also known as alkaline activated concrete, can be synthesized by activating recycled material such as fly ash and slag that can be used for repair, a kind of green building materials to reduce its carbon footprint (Dahou et al. 2016; Doguparti 2015; Jaffar et al. 2016). Different studies were conducted to investigate the applicability of using a geopolymer in different applications. For instant, geopolymer mortar was used to repair reinforced concrete (Geraldo et al. 2018; Sharkawi et al. 2020). It promoted 30 MPa after one day and had good adhesion to the concrete surface, which is essential to efficiently repair material (Geraldo et al. 2018). Moreover, it was used as a coating to protect the structures from the environmental condition. It was used to protect the reinforced concrete's corrosion and exhibited a good adhesion and excellent anticorrosive properties (Aguirre-Guerrero et al. 2017; Zhang et al. 2010). Thus, a geopolymer has the potential to be a good solution for repairing steel H-pile since, to date, no study has been carried out to investigate the behavior of the corroded steel H-pile encased with a geopolymer concrete jacket by either experimental work or numerical method.

The finite-element (FE) method offers an approach to investigate H piles' behavior encased with a concrete jacket. To date, 3D printing hasn't been implemented for repairing purposes. Thus, the simulating models using LS-DYNA software are better to understand the behavior of such a new repair method.

This paper presents a validated FE model of corroded full-scale steel H-pile against the experimental results to investigate the effects of concrete encasement layers and axial capacity. In addition, four large-scale, severely corroded steel H-pile repaired using concrete encasement. Among four, one was repaired with full concrete encasement (i.e., full concrete depth) which was carried out as a reference for comparison purposes, whereas other remaining specimens were repaired with a layered encasement, with different coefficient of friction between the concrete layers to be as the main parameter.

2. CORRODED STEEL H-PILE FE MODELING AND VALIDATION

2.1. FE MODELLING

The model was first validated against the experimental works conducted by Amro and ElGawady (2019) and Abdulazeez et. al. (2020) on severely corroded steel H-pile tested under axial compression. The tested steel H-pile was (HP 10x42) with a length of 120 in, a reduced thickness in the web and flange of 70%, 50%, respectively, and corrosion extension of 12 in with a rectangular void in web to simulate the severe corrosion. The flanges and web locally yielded at 152 kips, which triggered global buckling, and the load dropped abruptly. The load dropped abruptly until a displacement of 10.67 mm (0.43 in.) (Figure 2).

The model was developed using LS-DYNA software. The steel H-pile was simulated using Belytsehko-Tsay four-node shell elements with 6 degrees of freedom per node. The steel H-pile, the selected type of shell element, considers the geometrical nonlinearity to express the local buckling behavior accurately. Sensitivity analyses were conducted to determine the optimum sizes of the different elements. The final model had 5,128 elements and 5,596 nodes (Figure 1).

Material model 003-plastic_kinematic was used to model the steel H pile in LS-DYNA. This material model considers the steel as elastoplastic material, which can be defined using: (1) the elastic modulus, E; (2) the yield stress; and (3) Poisson's ratio. It has the option of including strain-hardening effects using a linear relationship for plastic behavior. Table 1 summarizes the properties of the simulated steel H-pile. The material properties were determined from tensile coupon tests (Abdulazeez et al. 2019). Moreover, the corroded region's geometric imperfections were included by reducing the thickness and simulating the void and the cuts (Figure 1).

Table 1: Mechanical properties of the steel H-pile (Abdulazeez et al. 2019).

Tensile modulus (ksi)	Yield strength (ksi)	Poisson's ratio
29,000	54	0.3

Using reduced integration formulation for the solid, shell, and thick-shell elements while decreasing the solution time can cause hourglass deformation. Internal hourglass forces are applied to resist the hourglass mode deformation (Kosloff and Frazier 1978) to avoid such a deformation mode. LS-DYNA uses hourglass coefficients

ranging from 0.03 to 0.10 to supersede the hourglass deformation. However, the energy of the added forces is deduced from the physical energy of the system. Therefore, using minimal hourglass energy while minimizing or preventing hourglass deformation is required to approach an accurate FE solution. Based on the current study's iterative process, an hourglass coefficient of 0.03 was found to be adequate to avoid hourglass deformations. NODE_TO_SURFACE contact elements were used between the loading and base plates and the steel H-pile, with a coefficient of friction of 1.0; therefore, the two nodes were forced to experience the same translations.

2.2. FE VALIDATION RESULTS

The FE model accurately predicted the steel H-piles's axial capacity versus axial shortening relations (Figure 2). The FE model predicted 94% of the steel H-pile's experimental ultimate axial capacity and 95.6% of the experimental ultimate axial shortening. Both the FE model and experimental work showed a high-stress concentration in the corroded region with internal and external wrinkling (Figure 3 and 4).

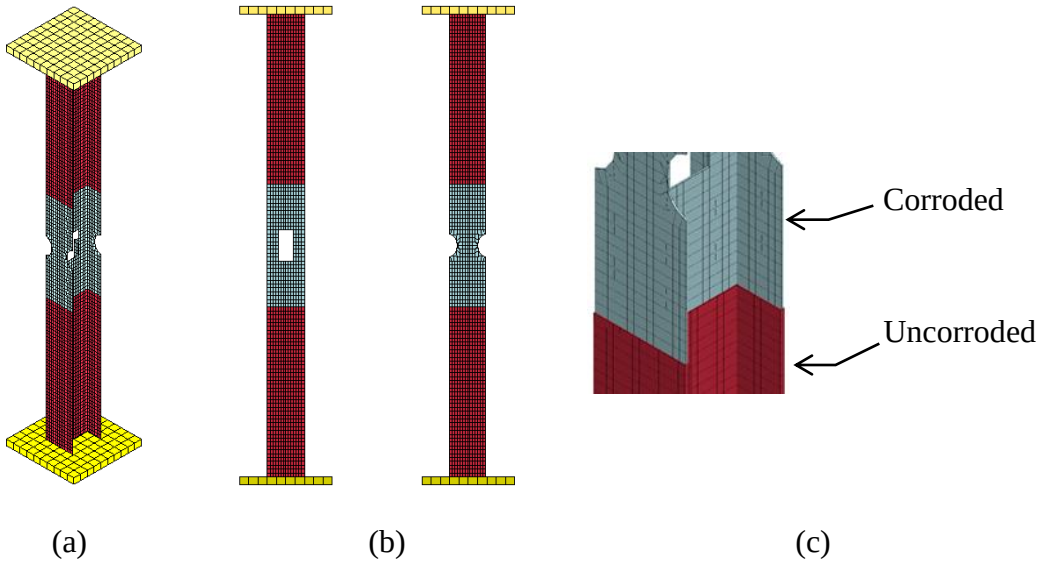

Figure 1: FE model parts (a) 3D view, (b) side views, and (c) thickness reduction simulation.

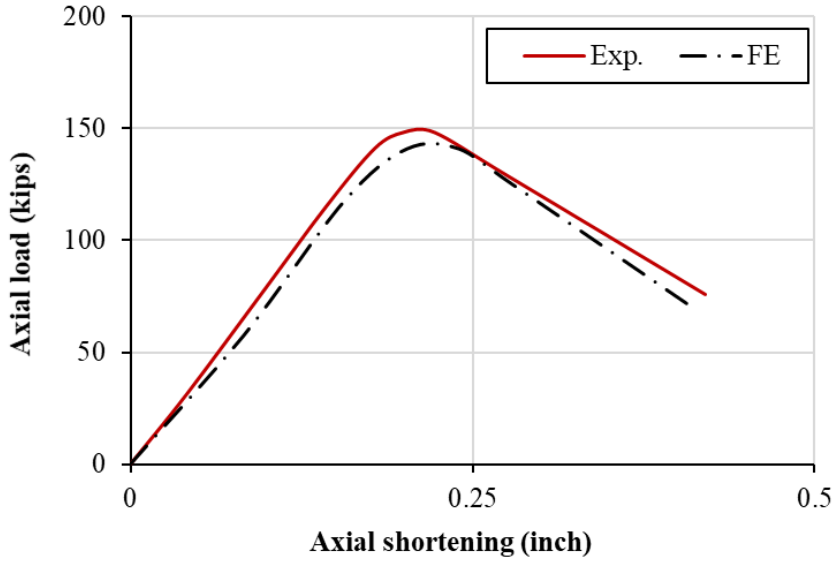

Figure 2: Experimental versus FE axial shortening-load backbone curves. (Experimental data from Amro and ElGawady 2019).

Figure 3: Experimental test failure mode

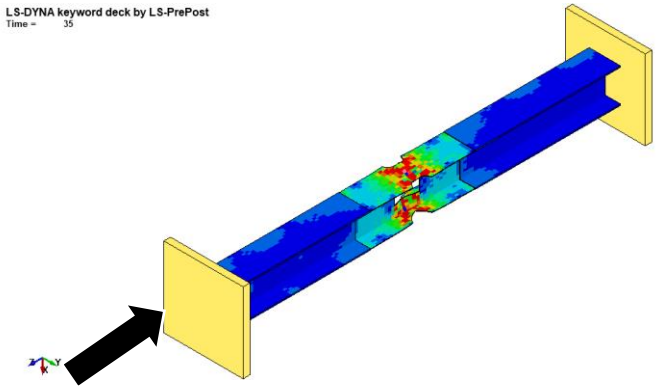

(a)

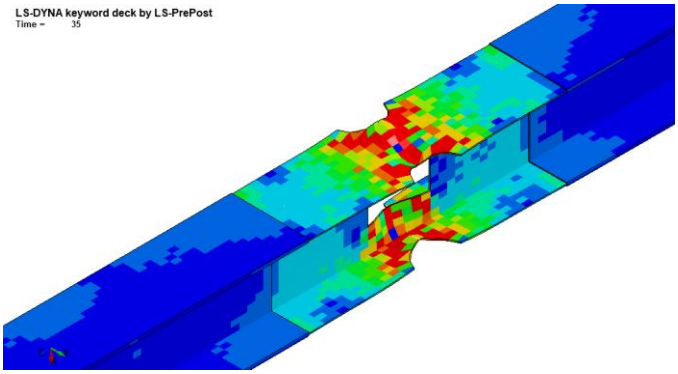

(b)

Figure 4: FE simulation failure mode.

3. REPAIRED STEEL H-PILE FE MODELLING

3.1. FE PARAMETRIC STUDY

The validated model was used to examine the failure mode, axial strength capacity, and friction coefficient (μ) of four FE models under axial compression. One FE model having a full concrete encasement (named model HP1-Full). The other three were having layered concrete encasements imitating the 3D printing scenario. Table 2 summarized the parametric studies of the FE models. The compressive strength was taken as an average of 6.0 ksi based on the experimental results (Fareh et al., 2020). The first segment is the letters HP referring to the steel H piles, followed by the letter F, referring to the full encasement or L, referring to the layered encasement and the layered concrete's coefficient. For example, model HP-L-0.5 was a reference steel H-pile encased with layered concrete with a friction coefficient of 0.5.

Table 2: Parametric studies of the FE models.

Model name	Encasement type	No. of layers	Thickness/depth (in)	μ between concrete and steel	μ between concrete layers
HP-F	Full encasment	1.0	32	0.6	-
HP-L-0.5	Layered encasment	16	2”@16 layers	0.6	0.5
HP-L-0.6				0.6	0.6
HP-L-0.7				0.6	0.7

3.2. MODEL GEOMETRY

The geometric properties and material properties of the repaired steel H-pile are illustrated in section FE modeling. A sensitivity analysis was conducted to determine the different element sizes. The element type and size were determined according to a sensitivity study, and the final FE model had 41,862 elements and 35,857 nodes. Figure 6 shows the final FE model of the different simulated repair steel H-pile.

3.3. MATERIAL MODELS

3.3.1. Concrete. Release III of the Karagozian and Case (K&C) was used to model the concrete material. The model was developed based on the theory of plasticity and had three shear failure surfaces (1) yield, (2) maximum, and (3) residual shear (Malvar et al. 1997). Several investigators used this material model to predict concrete structures' performance under lateral cyclic loads (Abdelkarim and ElGawady 2014; Ryu et al. 2013; Youssf et al. 2014). The automatic option was used to generate all the model parameters, i.e., given the uniaxial unconfined compressive strength f_c' ; the model is able to create all the constants required for the finite element analysis.

The concrete encasement was modeled using constant-stress solid elements, which uses single-point integration, which reduces the computational time over the full integration element with reasonable accuracy.

3.3.2. Steel H-pile. The material model for the steel H-pile was used as discussed in Section 2.1.

3.4. BOUNDARY CONDITION AND LOADING

Boundary conditions were modeled to represent the test set-up at the supports. At the fixed end of the pile, translation was restrained in three perpendicular directions. At the jacking end, translation was restrained in the global X and Y directions, but the pile was free to translate in the axial, global Z. The piles were loaded by imposing an axial displacement at one end to simulate the action of the hydraulic jack in the experimental program.

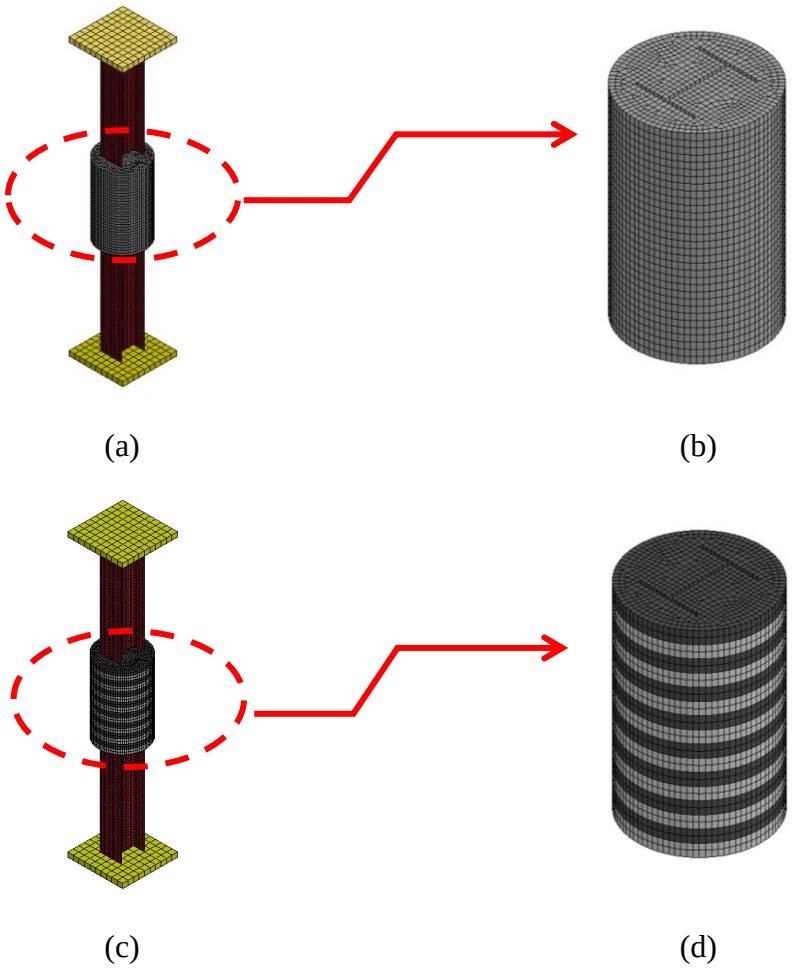

Figure 5: FEM of the repaired H piles encased with: (a) Full layered and (b) layered concrete.

Automatic-Surface-to-surface contact elements were used to simulate the interface between the concrete encasement and the steel H-pile. In this approach, the master and slave surfaces are generated internally within LS-DYNA from the parts ID's given for each surface. Node-to-surface contact elements were used between the loading plates, and the steel pile ends.

The friction coefficient of the contact between the concrete and steel H pile was 0.6, while it was 0.5, 0.6, and 0.7 between layered concrete based on the coefficient of friction between layered concrete reported from the slant shear test (Fareh et al. 2020). Thus, this study predicts H-pile's behavior encased with layered concrete with different coefficient values and compared it with H pile encased with full-layered concrete.

4. RESULTS AND DISCUSSION

4.1. FAILURE MODES

Figure 6 shows the failure modes of the steel H-pile encased with full concrete. In general, the crack initiation started in the middle region of the concrete encasement around the corroded steel H-pile part in the steel/concrete interface at the flanges tips. The reason is due to the small concrete thickness that triggered stress concentration in that area. The cracks were propagated laterally and longitudinally towards the concrete encasement's outer face at 80% of the ultimate strength and axial shortening, and debonding followed by separation occurs at the contact interface (Figure 6 b and d). The steel H-pile failure mode is approximately the same as the tested virgin steel H-pile

without concrete encasement, represented by localized buckling and web and flanges wrinkling (Figure 6 c).

Figure 7 shows the FE modes of H pile failure encased with layered concrete having a friction coefficient of 0.5. In general, the crack initiation started in the concrete middle region encasing the corroded steel H-pile part in the steel/concrete interface at the flanges tips. Concrete encasement lateral expansion is followed by layered debonding and separation. However, the cracks were located at the middle region and not extended longitudinally along with the concrete encasement, which is different from the full encasement case. The cracks propagated radially after that at 50% of the ultimate strength and axial shortening, and debonding followed by separation occurs at the contact interface (Figure 7 b and d). The steel H-pile failure mode is approximately the same as the full concrete encasement, represented by localized buckling and web and flanges inward and outward wrinkling (Figure 7 c).

Likewise, for steel H-pile encased with layered concrete, a friction coefficient of either 0.6 or 0.7 same phenomena were observed. However, the radially cracked region's location localized within one-third of the total layered concrete encasement (Figs. 8 and 9), which is different from the investigated specimen with a 0.5 coefficient of friction. The steel H-pile failure mode is approximately the same as the full concrete encasement, represented by localized buckling and web and flanges inward and outward wrinkling (Figs. 8(c) and 9(c)).

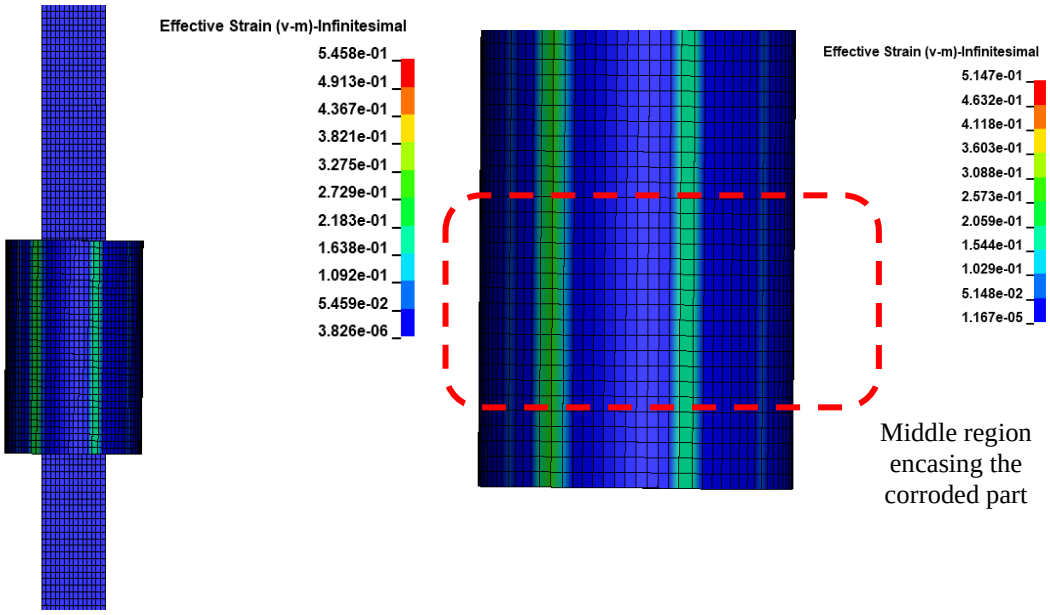

(a) (b)

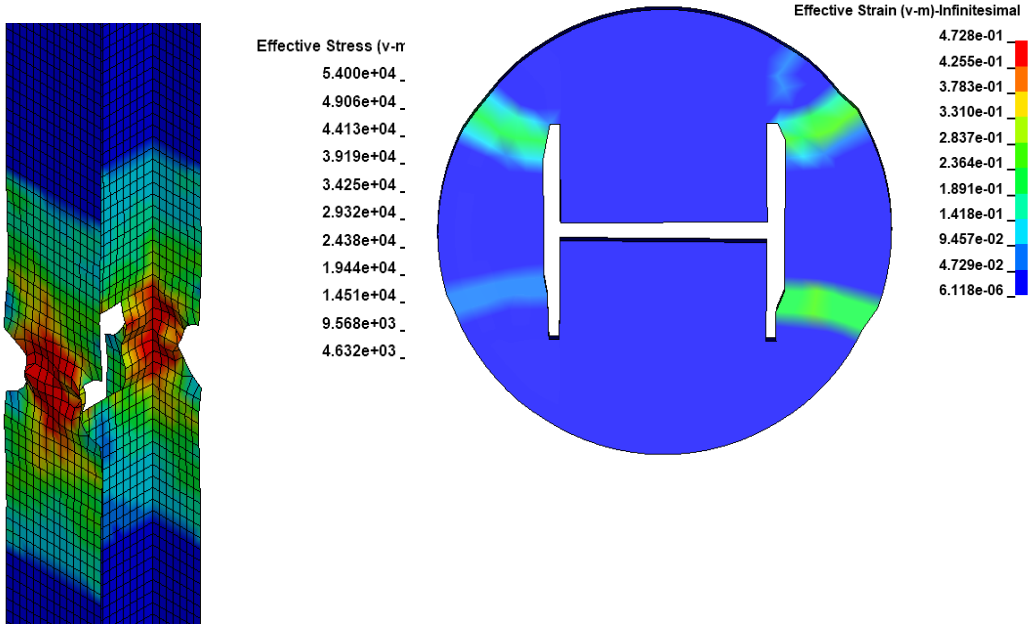

(c) (d)

Figure 6: Full layered encasement steel H-pile.

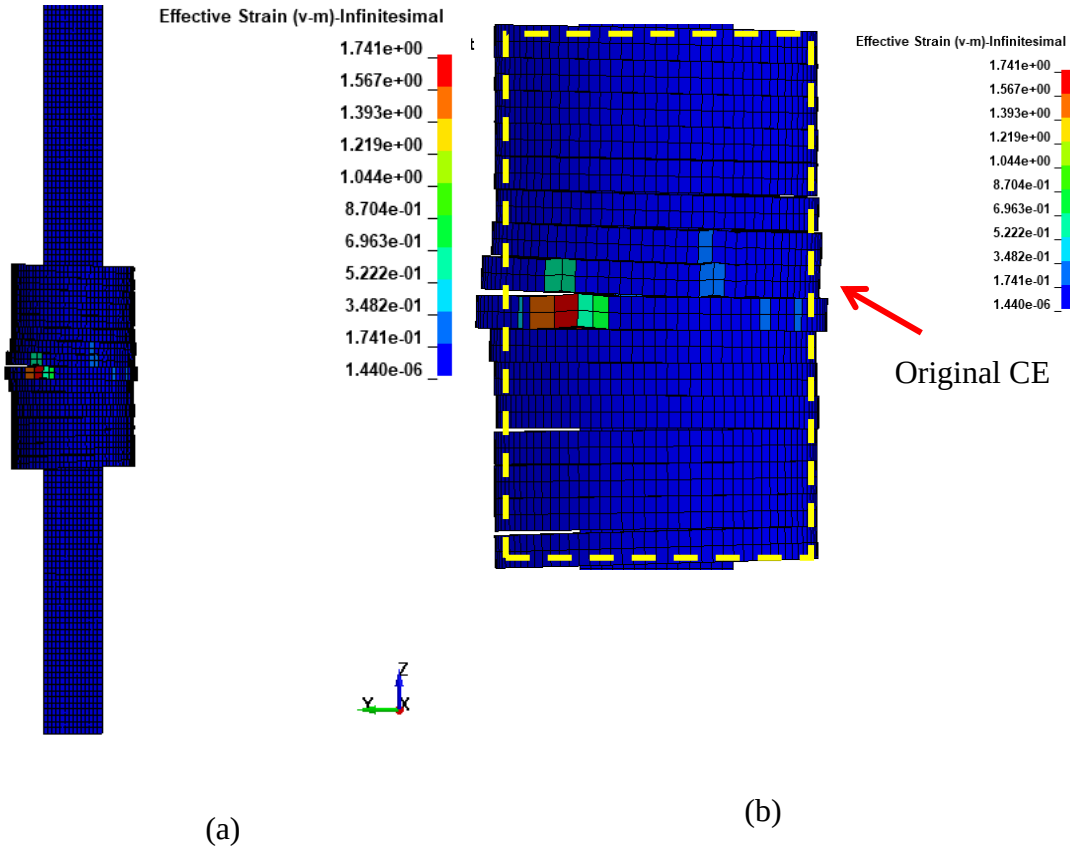

(a) (b)

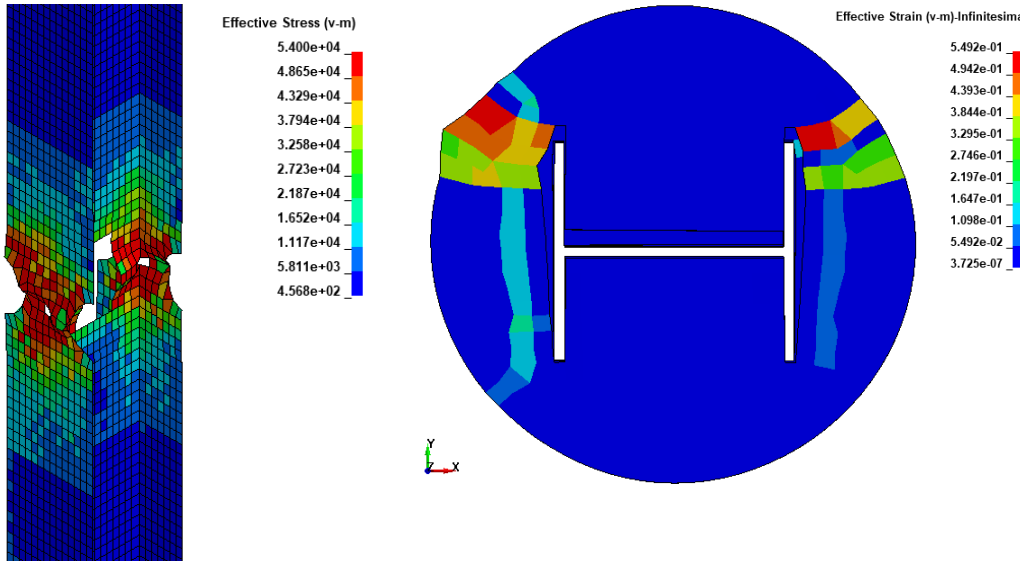

(c) (d)

Figure 7: Friction coefficients (μ) = 0.5.

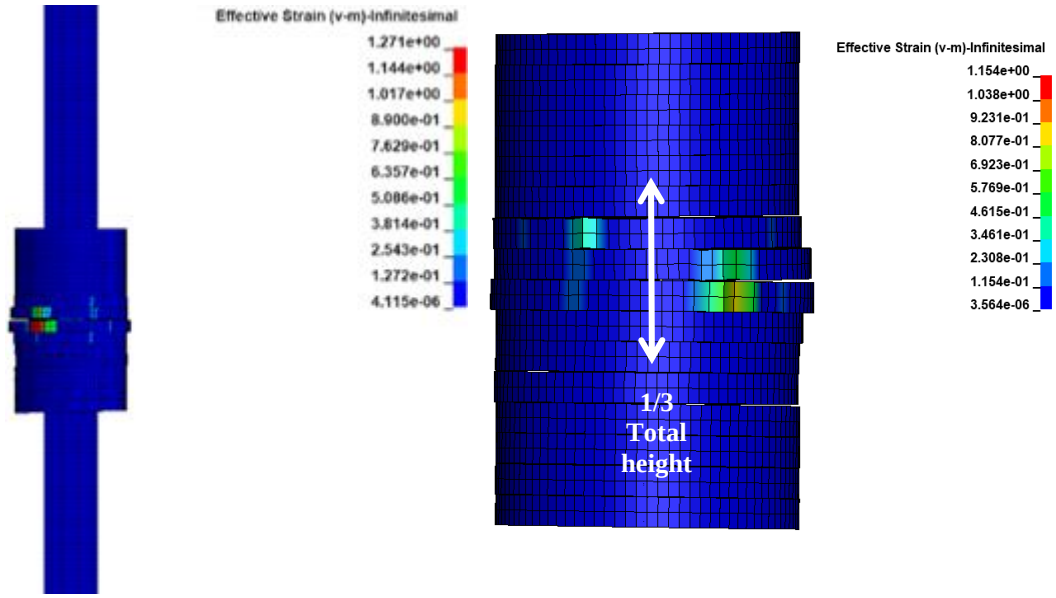

(a) (b)

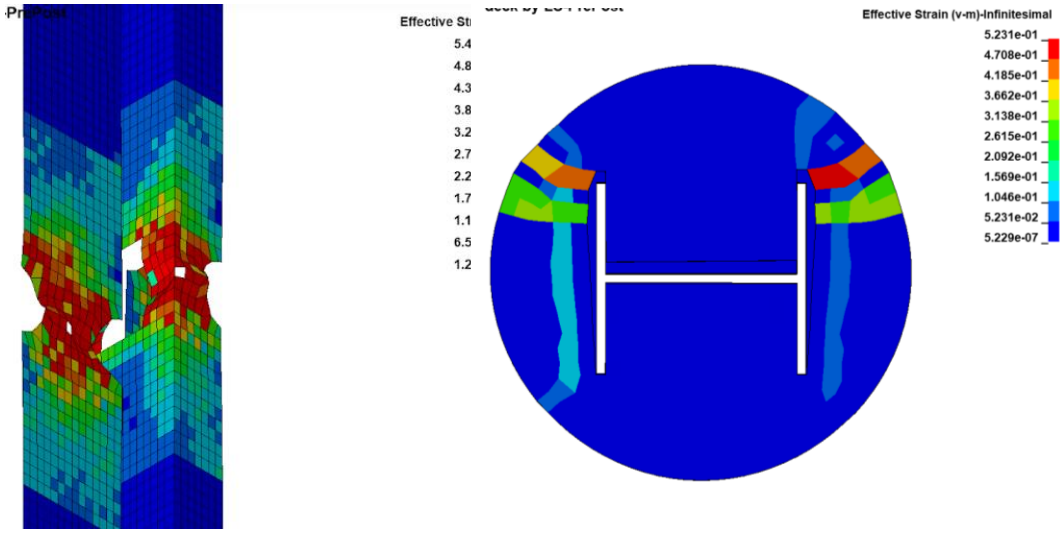

(c) (d)

Figure 8: Friction coefficients (μ) = 0.6.

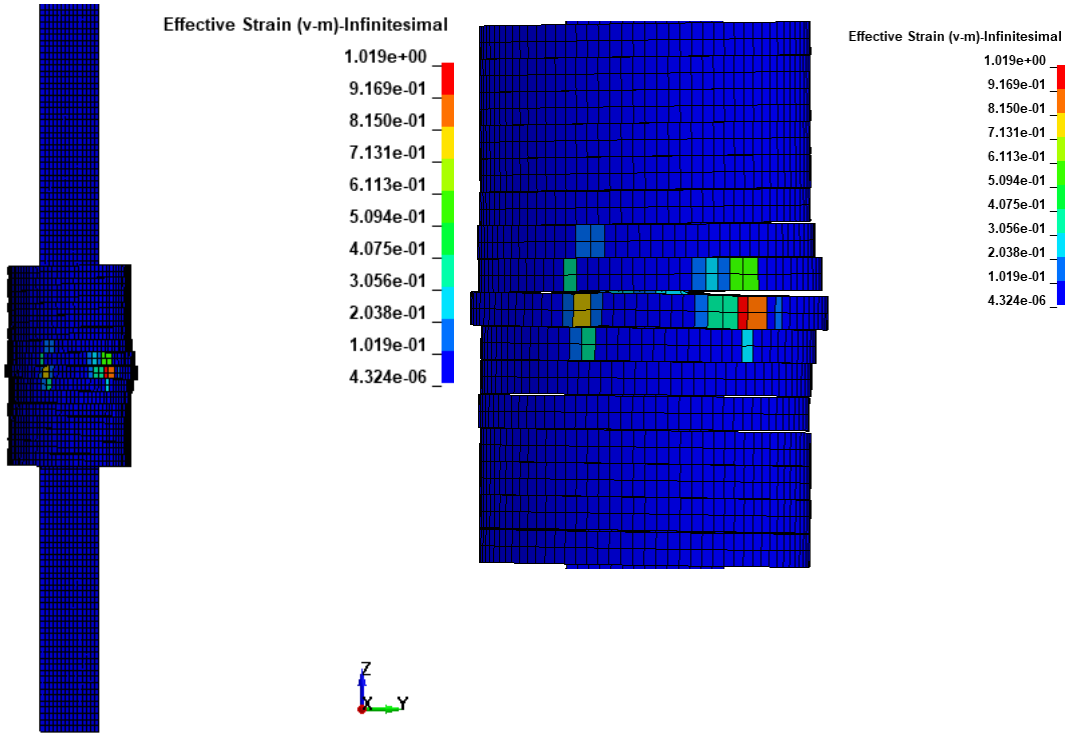

(a) (b)

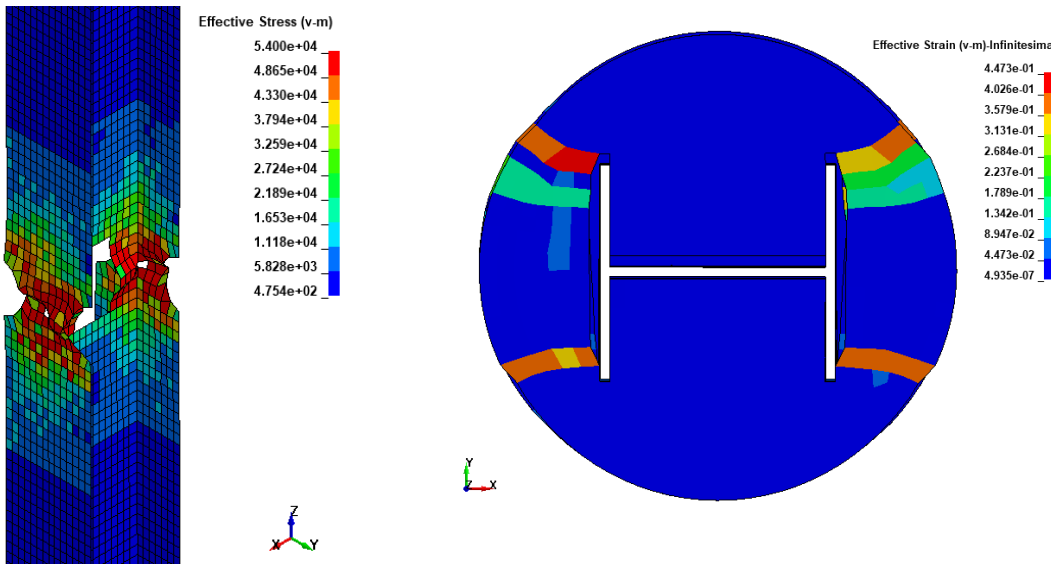

(c) (d)

Figure 9: Friction coefficients (μ) = 0.7.

4.2. AXIAL CAPACITY AND PERFORMANCE

Table 3 shows the FE models' axial capacities, virgin steel H-pile, repaired steel-H pile having either full or layered encasement concrete. The repair corroded steel H-pile achieved relatively higher axial capacity and better performance than the virgin tested one. The repaired Steel H-piles' axial capacity was higher by 13% more than the virgin one steel H-pile. The axial capacities results for repaired steel H piles encased with layered concrete were very close to steel H-pile encased with full concrete indicating a slight enhancement in the strength gain by using a 3D printing method. This achievement can be enhanced highly by implementing embedded shear connectors into the layered CE or providing some confinement as approved experimentally (Abdulazeez et al. 2019).

It is worth noticing that the repaired steel H-piles with layered concrete encasement axial load-shortening showed a change in the initial stiffness at 0.125 in. due to the early cracks localization and propagation (Figure 10).

Table 3: Axial capacity of the FE models.

Model No.	HP Validated	HP-F	HP-L-0.5	HP-L-0.6	HP-L-0.7
Axial capacity (kips)	141	155	144	152	162

4.3. COEFFICEINT OF FRICTION

Figure 10 shows the axial capacity vs. axial shortening (i.e., displacement) for the repaired steel H-piles encased with full concrete and layered concrete having friction coefficients of 0.5, 0.6, and 0.7 between the concrete layer. In general, as the friction

coefficient increased, the axial peak capacity increased and the concrete encasement damage was reserved within the middle region of one-third of the total encasement height. The axial capacity for HP-F, HP-L-0.5, HP-L-0.6, and HP-L-0.7 was 155, 144, 152, and 162 kips, respectively. With increasing the frictional coefficient, the bond between layered concrete increased, causing less debonding. Due to an increase in friction coefficient, there is an increase in the shear force between the layers, which subsequently increased the axial capacity.

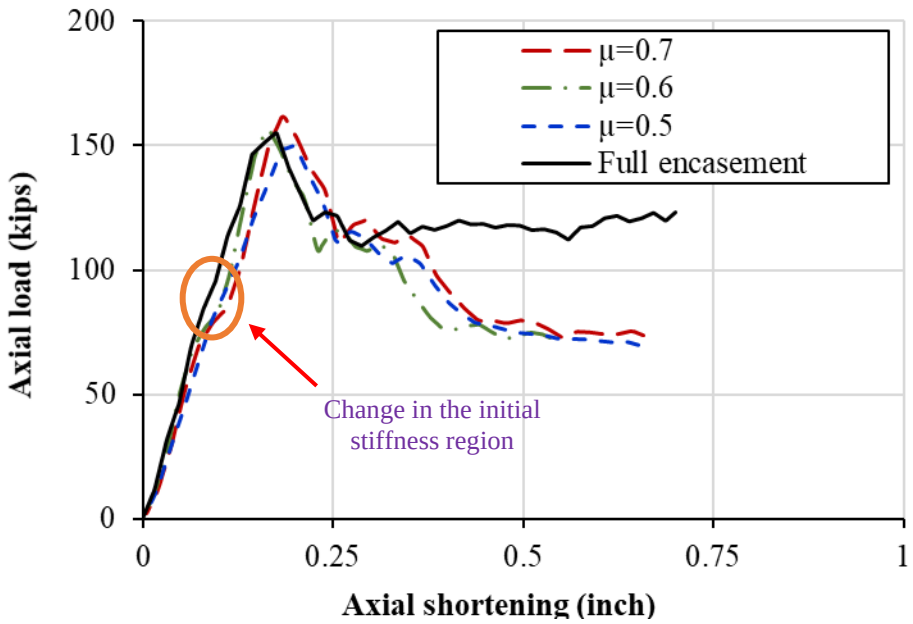

Figure 10: Axial load (kips) vs. axial shortening (inch) for H pile encased with layered concrete having different friction coefficients.

It is worth noticing that a repaired steel H-pile encased with layered concrete with a friction coefficient of 0.7 was higher by 13% than a repaired steel H-pile encased with full concrete. The crack initiation discontinuity could explain this in the layered encasement compared to the full encasement (Figure 11). At a strain of 0.22 in./in. The

layered encasement concrete prevented the crack propagation from the middle of the concrete to the top. The bottom layers indicated that full contact between layers was maintained at the top and bottom of the concrete layers. Whereas at the same strain, the crack initiation occurred in the full encasement along with the full concrete depth, as shown in Figure 11b.

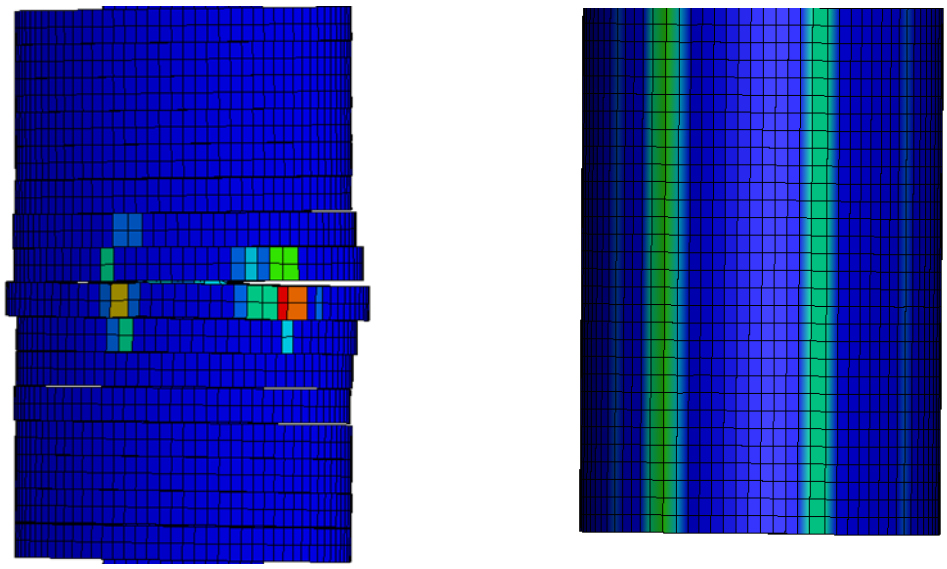

(a) (b)

Figure 11: Crack initiation phenomena for (a) layered encasement and (b) full encasement.

5. CONCLUSIONS

This study presents FE models of the corroded steel H-piles repaired using concrete two types of concrete encasement subjected to axial compression. Full encasement and layered encasement were investigated to mimic 3D printed concrete. In addition, the experimental results were used to validate severely corroded steel H-pile as

a virgin specimen for comparison purposes. Based on the validated model, parametric studies were conducted on the developed models to investigate the effect of the concrete encasement type in terms of the failure modes, obtained axial capacity, and coefficient of friction between the layers. Based on the parametric studies, the following conclusions can be drawn:

- For both concrete encasement types, the crack initiation occurred on the middle region of the concrete encasement around the corroded steel H-pile part in the steel/concrete interface at the flanges tips due to the stress concentration at that region.
- The failure mode of the repaired steel H-pile encased with either full or layered concrete, regardless of the friction coefficient between layers, was approximately the same as the tested virgin steel H-pile (i.e., without concrete encasement); localized buckling and web and flanges wrinkling took place.
- In general, the axial capacity of the repaired Steel H-piles was higher than the virgin one. It was higher by 13% more than the virgin steel H-pile.
- Debonding phenomena was observed for repaired steel H-pile encased with layered concrete regardless of values of the friction coefficients between layers.
- Increasing friction coefficients between layered concrete increased the axial capacities due to the increase of the shear force between layers. It was 144, 152, and 162 kips, for HP-L-0.5, HP-L-0.6, and HP-L-0.7, respectively.
- The axial capacity of the repaired steel H-pile encased with full concrete was higher than those encased with layered concrete having different friction coefficients

between layers except the repaired one having a friction coefficient of 0.7 which was explained by the discontinuity of the crack initiation observation.

REFERENCES

Abdelkarim, O. I., and ElGawady, M. A. (2014). "Analytical and Finite-Element Modeling of FRP-Concrete-Steel Double-Skin Tubular Columns." *Journal of Bridge Engineering*.

Abdulazeez, M. M., Ramadan, A., Sherstha, B., Gheni, A., Gomaa, E., Darwish, Y., and ElGawady, M. A. (2019). "Behavior and Repair of Corroded Steel H-Piles Phase I (Axial Behavior)."

Aguirre-Guerrero, A. M., Robayo-Salazar, R. A., and de Gutiérrez, R. M. (2017). "A novel geopolymer application: Coatings to protect reinforced concrete against corrosion." *Applied Clay Science*, 135, 437-446.

Dahou, Z., Castel, A., and Noushini, A. (2016). "Prediction of the steel-concrete bond strength from the compressive strength of Portland cement and geopolymer concretes." *Construction and Building Materials*, 119, 329-342.

Dawood, M., Karagah, H., Shi, C., Belarbi, A., Vipulanandan, C., Bae, S.-W., and Lee, S. (2017). "Repair systems for deteriorated bridge piles." University of Houston.

Doguparti, R. S. (2015). "A study on bond strength of geopolymer concrete." *International Journal of Civil Environmental, Structural, Construction and Architectural Engineering*, 9(3), 355-358.

Ehsani, M. (2009). "FRP super laminates present unparalleled solutions to old problems." *REINFORCED plastics*, 53(6), 40-45.

Geraldo, R. H., Teixeira, O. G., Matos, S. R., Silva, F. G., Gonçalves, J. P., and Camarini, G. (2018). "Study of alkali-activated mortar used as conventional repair in reinforced concrete." *Construction and Building Materials*, 165, 914-919.

Iskander, M. G., and Stachula, A. (2002). "Wave equation analyses of fiber-reinforced polymer composite piling." *Journal of Composites for Construction*, 6(2), 88-96.

Jaffar, M. I., Badaruzzaman, W. H. W., and Baharom, S. (2016). "Experimental tests on bending behavior of profiled steel sheeting dry board composite floor with geopolymer concrete infill." *Latin American Journal of Solids and Structures*, 13(2), 272-295.

Karagah, H., Dawood, M., and Belarbi, A. (2018). "Experimental Study of Full-Scale Corroded Steel Bridge Piles Repaired Underwater with Grout-Filled Fiber-Reinforced Polymer Jackets." *Journal of Composites for Construction*, 22(3), 04018008.

Karagah, H., Shi, C., Dawood, M., and Belarbi, A. (2015). "Experimental investigation of short steel columns with localized corrosion." *Thin-Walled Structures*, 87, 191-199.

Liu, X., Nanni, A., Silva, P. F., and Laboube, R. A. (2001). "Rehabilitation of steel bridge columns with FRP composite materials." *Proc., CCC*, 10-12.

Ma, G., Wang, L., and Ju, Y. (2018). "State-of-the-art of 3D printing technology of cementitious material—An emerging technique for construction." *Science China Technological Sciences*, 61(4), 475-495.

Malvar, L. J., Crawford, J. E., Wesevich, J. W., and Simons, D. (1997). "A plasticity concrete material model for DYNA3D." *International Journal of Impact Engineering*, 19(9), 847-873.

Ngo, T. D., Kashani, A., Imbalzano, G., Nguyen, K. T., and Hui, D. (2018). "Additive manufacturing (3D printing): A review of materials, methods, applications and challenges." *Composites Part B: Engineering*, 143, 172-196.

Rahul, A., Santhanam, M., Meena, H., and Ghani, Z. (2019). "Mechanical characterization of 3D printable concrete." *Construction and Building Materials*, 227, 116710.

Ryu, D., Wijeyewickrema, A. C., ElGawady, M. A., and Madurapperuma, M. (2013). "Effects of tendon spacing on in-plane behavior of posttensioned masonry walls." *Journal of Structural Engineering*, 140(4), 04013096.

Sharkawi, A., Taman, M., Afefy, H. M., and Hegazy, Y. "Efficiency of geopolymer vs. high-strength grout as repairing material for reinforced cementitious elements." *Proc., Structures*, Elsevier, 330-342.

Shi, C., Karagah, H., Dawood, M., and Belarbi, A. (2014). "Numerical investigation of H-shaped short steel piles with localized severe corrosion." *Engineering Structures*, 73, 114-124.

Wan, B., Foley, C. M., Ainge, S. W., and Nguyen, C. (2013). "Procedures, Cost and Effectiveness for Deteriorated Bridge Substructure Repair."

Wipf, T. J., Fanous, F., Klaiber, F., and Eapen, A. (2003). "Evaluation of Appropriate Maintenance, Repair and Rehabilitation Methods for Iowa Bridges." *Final Report, Iowa DOT Project TR-429*.

Youssf, O., ElGawady, M. A., Mills, J. E., and Ma, X. (2014). "Finite element modelling and dilation of FRP-confined concrete columns." *Engineering Structures*, 79, 70-85.

Zhang, Z., Yao, X., and Zhu, H. (2010). "Potential application of geopolymers as protection coatings for marine concrete: I. Basic properties." *Applied clay science*, 49(1-2), 1-6.

SECTION

3. CONCLUSIONS AND RECOMMENDATIONS

3.1. CONCLUSIONS

This thesis presented the behavior of steel H-piles encased with layered concrete jacket using AAM to simulate 3D printing technology. The applicability of using class C fly ash based AAM for different application towered 3D printing was investigated at the beginning. Different tests were conducted to study the fresh (i.e., open time and deformation tests) and hardened properties (i.e., compressive strength, bond strengths, and microstructural analysis) of AAM through studying the effect of W/FA, Alk/FA, and SS/SH ratios. Based on the results that were reported, the research findings led to the following conclusions:

- A wide range of open time was achieved (i.e., it ranged from 2.5 to 31 minutes) which could be applicable for different 3D printing applications.
- A wide range of CTs was selecting, CTs ranged from 1.0 to 60 minutes, to offer flexibility to the construction industry to select the target CT based on the 3D printed structure. With increasing CT between loads, the deformation decreased due to the material's strength gained through time.
- In terms of the compressive strength, anisotropic behavior was observed of 3DPC specimens. The compressive strength of 3DPC specimens tested in the X-direction was higher by 0.03 to 22.7% than 3DPC tested in Z-direction.

- With increasing CT between adding the subsequent layers, the compressive strength of 3DPC specimens was decreased regardless of the testing direction. The reduction in the compressive strength reached up 46.7 % with CT of 24 hours compared with 1.0 minutes.
- Bond strength was relatively high for CTs ranged from 2.5 to 60 minutes as compared with CT of 24 hours. Thus, CT is a significant factor effect on bond strength. As the CT increased the bond strength decreased.
- The failure mode of 3DPC specimens having CT from 2.5 to 60 minutes was relatively close to the full specimens indicated that class C FA showed a relatively high bond strength.

Based on the previously reported results, and since Class C FA was successfully developed in simulating 3D printing, FE models were developed and validated against experimental results of a large scale column collected from the literature to investigate the applicability of repaired corroded steel H- piles encased with layered concrete. Two types of concrete encasement were investigated, full encasement (for comparison purpose) and layered encasement to mimic 3D printed concrete. The validated corroded steel H-pile which was modeled without concrete encasement was implemented to conduct a parametric study investigating the effect of the concrete encasement type in terms of the obtained axial capacity, coefficient of friction between the layered, and the failure modes. The FE proposed models were able to predict the behaviors of the large-scale columns steel H-piles encased with either full or layered concrete. Based on the FE models behavior, it is concluded that:

- The failure mode of the repaired corroded steel H-piles was the same for both concrete encasement types; in other words, the crack initiation occurred on the middle region of the concrete encasement around the corroded steel H-pile part due to the stress concentration at that region.
- Localized buckling and web and flanges wrinkling took place were observed of the repaired steel H-piles regarding the encasement type which was the same as the tested virgin steel H-pile without repair.
- The axial capacity of the repaired steel H-piles was higher than the virgin one. It was higher by 13% more than the virgin steel H-pile.
- Debonding phenomena was observed for repaired steel H-pile encased with layered concrete.
- With increasing friction coefficients between layered concrete, the axial capacities increased as well due to the increase of the shear force between layers. It was 144, 152, and 162 kips, for HP-L-0.5, HP-L-0.6, and HP-L-0.7, respectively.
- The axial capacity of the repaired steel H-pile encased with full concrete was higher than those encased with layered concrete having different friction coefficients between layers except the repaired one having a friction coefficient of 0.7 which was explained by the discontinuity of the crack initiation observation.

3.2. RECOMMENDATIONS

This research mainly focused on investigating the applicability of using class C FA based geopolymer mortar in simulating 3D printing and subsequently repairing corroded steel H-piles. Thus, no real 3D printing was applied. Future work can be

focused on using a printer to mimic reality. Rheological properties of class C FA-based geopolymer mortar are crucial, thus additional work should be carried out for the best understanding of the fresh properties. Repairing steel H-piles using a 3D-printer can be carried further investigated in order to better out for the best understanding of the failure mode. Using 3D printing technology for repairing purposes could be promised and this achievement can be enhanced highly by implementing embedded shear connectors into the layered concrete encasement or providing some confinement.

BIBLIOGRAPHY

Abdulazeez, M. M., Ramadan, A., Sherstha, B., Gheni, A., Gomaa, E., Darwish, Y., and ElGawady, M. A. (2019). "Behavior and Repair of Corroded Steel H-Piles Phase I (Axial Behavior)."

ASTM-F2792-10 "Standard Terminology for Additive Manufacturing Technologies." *ASTM International*.

Bong, S. H., Nematollahi, B., Nazari, A., Xia, M., and Sanjayan, J. G. "Fresh and hardened properties of 3D printable geopolymer cured in ambient temperature." *Proc., RILEM International Conference on Concrete and Digital Fabrication*, Springer, 3-11.

Davidovits, J. (2013). "Geopolymer cement." *A review. Geopolymer Institute, Technical papers*, 21, 1-11.

Dawood, M., Karagah, H., Shi, C., Belarbi, A., Vipulanandan, C., Bae, S.-W., and Lee, S. (2017). "Repair systems for deteriorated bridge piles." University of Houston.

Department of the Army, D. o. t. A. (1991). "Pile construction." Department of the Army US, Washington, DC: Headquarters.

Duxson, P., and Provis, J. L. (2008). "Designing precursors for geopolymer cements." *Journal of the American Ceramic Society*, 91(12), 3864-3869.

Ehsani, M. (2009). "FRP super laminates present unparalleled solutions to old problems." *REINFORCED plastics*, 53(6), 40-45.

FHWA (2015). "National Bridge Inventory." *U.S. Department of Transportation, Federal Highway Administration*.

Gao, W., Zhang, Y., Ramanujan, D., Ramani, K., Chen, Y., Williams, C. B., Wang, C. C., Shin, Y. C., Zhang, S., and Zavattieri, P. D. (2015). "The status, challenges, and future of additive manufacturing in engineering." *Computer-Aided Design*, 69, 65-89.

Georgia Department of Transportation (2012). "Bridge Structure Maintenance and Rehabilitation Repair Manual."

Hager, I., Golonka, A., and Putanowicz, R. (2016). "3D printing of buildings and building components as the future of sustainable construction?" *Procedia Engineering*, 151, 292-299.

Jha, K. N. (2012). *Formwork for concrete structures*, Tata McGraw Hill Education Private Limited.

Karagah, H., Dawood, M., and Belarbi, A. (2018). "Experimental Study of Full-Scale Corroded Steel Bridge Piles Repaired Underwater with Grout-Filled Fiber-Reinforced Polymer Jackets." *Journal of Composites for Construction*, 22(3), 04018008.

Kashani, A., and Ngo, T. "Optimisation of mixture properties for 3D printing of geopolymer concrete." *Proc., ISARC. Proceedings of the International Symposium on Automation and Robotics in Construction*, IAARC Publications, 1-8.

Kazemian, A., Yuan, X., Cochran, E., and Khoshnevis, B. (2017). "Cementitious materials for construction-scale 3D printing: Laboratory testing of fresh printing mixture." *Construction and Building Materials*, 145, 639-647.

Khan, M. S., Sanchez, F., and Zhou, H. (2020). "3-D printing of concrete: Beyond horizons." *Cement and Concrete Research*, 133, 106070.

Kosson, M., Brown, L., and Sanchez, F. (2020). "Early-Age Performance of 3D Printed Carbon Nanofiber and Carbon Microfiber Cement Composites." *Transportation Research Record*, 2674(2), 10-20.

Le, T. T., Austin, S. A., Lim, S., Buswell, R. A., Gibb, A. G., and Thorpe, T. (2012). "Mix design and fresh properties for high-performance printing concrete." *Materials and structures*, 45(8), 1221-1232.

Le, T. T., Austin, S. A., Lim, S., Buswell, R. A., Law, R., Gibb, A. G., and Thorpe, T. (2012). "Hardened properties of high-performance printing concrete." *Cement and Concrete Research*, 42(3), 558-566.

Liu, X., Nanni, A., Silva, P. F., and Laboube, R. A. (2001). "Rehabilitation of steel bridge columns with FRP composite materials." *Proc., CCC*, 10-12.

Ma, G., Li, Z., and Wang, L. (2018). "Printable properties of cementitious material containing copper tailings for extrusion based 3D printing." *Construction and building materials*, 162, 613-627.

Ma, G., Li, Z., Wang, L., Wang, F., and Sanjayan, J. (2019). "Mechanical anisotropy of aligned fiber reinforced composite for extrusion-based 3D printing." *Construction and Building Materials*, 202, 770-783.

Ma, G., Wang, L., and Ju, Y. (2018). "State-of-the-art of 3D printing technology of cementitious material—An emerging technique for construction." *Science China Technological Sciences*, 61(4), 475-495.

Malaeb, Z., Hachem, H., Tourbah, A., Maalouf, T., El Zarwi, N., and Hamzeh, F. (2015). "3D concrete printing: machine and mix design." *International Journal of Civil Engineering*, 6(6), 14-22.

Marchment, T., Xia, M., Dodd, E., Sanjayan, J., and Nematollahi, B. "Effect of delay time on the mechanical properties of extrusion-based 3D printed concrete." *Proc., Proceedings of the International Symposium on Automation and Robotics in Construction, Taipei, Taiwan*.

Nematollahi, B., Vijay, P., Sanjayan, J., Nazari, A., Xia, M., Naidu Nerella, V., and Mechtcherine, V. (2018). "Effect of Polypropylene Fibre Addition on Properties of Geopolymers Made by 3D Printing for Digital Construction." *Materials*, 11(12), 2352.

Nerella, V. N., Hempel, S., and Mechtcherine, V. (2019). "Effects of layer-interface properties on mechanical performance of concrete elements produced by extrusion-based 3D-printing." *Construction and Building Materials*, 205, 586-601.

Ngo, T. D., Kashani, A., Imbalzano, G., Nguyen, K. T., and Hui, D. (2018). "Additive manufacturing (3D printing): A review of materials, methods, applications and challenges." *Composites Part B: Engineering*, 143, 172-196.

Panda, B., Paul, S. C., Hui, L. J., Tay, Y. W. D., and Tan, M. J. (2017). "Additive manufacturing of geopolymer for sustainable built environment." *Journal of cleaner production*, 167, 281-288.

Panda, B., Paul, S. C., Mohamed, N. A. N., Tay, Y. W. D., and Tan, M. J. (2018). "Measurement of tensile bond strength of 3D printed geopolymer mortar." *Measurement*, 113, 108-116.

Panda, B., Paul, S. C., and Tan, M. J. (2017). "Anisotropic mechanical performance of 3D printed fiber reinforced sustainable construction material." *Materials Letters*, 209, 146-149.

Panda, B., and Tan, M. J. (2018). "Experimental study on mix proportion and fresh properties of fly ash based geopolymer for 3D concrete printing." *Ceramics International*, 44(9), 10258-10265.

Papachristoforou, M., Mitsopoulos, V., and Stefanidou, M. (2018). "Evaluation of workability parameters in 3D printing concrete." *Procedia Structural Integrity*, 10, 155-162.

Paul, S. C., Tay, Y. W. D., Panda, B., and Tan, M. J. (2018). "Fresh and hardened properties of 3D printable cementitious materials for building and construction." *Archives of civil and mechanical engineering*, 18(1), 311-319.

Rahul, A., Santhanam, M., Meena, H., and Ghani, Z. (2019). "Mechanical characterization of 3D printable concrete." *Construction and Building Materials*, 227, 116710.

Sanjayan, J. G., Nematollahi, B., Xia, M., and Marchment, T. (2018). "Effect of surface moisture on inter-layer strength of 3D printed concrete." *Construction and Building Materials*, 172, 468-475.

Soliman, K., Arafa, A., and Elrakib, T. M. (2013). "Review of design codes of concrete encased steel short columns under axial compression." *HBRC journal*, 9(2), 134-143.

Stauffer, S. T. (2016). "Performance Assessment of Deteriorated and Repairted Steel HP Piles."

Tay, Y. W. D., Panda, B., Paul, S. C., Noor Mohamed, N. A., Tan, M. J., and Leong, K. F. (2017). "3D printing trends in building and construction industry: a review." *Virtual and Physical Prototyping*, 12(3), 261-276.

Tay, Y. W. D., Ting, G. H. A., Qian, Y., Panda, B., He, L., and Tan, M. J. (2019). "Time gap effect on bond strength of 3D-printed concrete." *Virtual and Physical Prototyping*, 14(1), 104-113.

Wan, B., Foley, C. M., Ainge, S. W., and Nguyen, C. (2013). "Procedures, Cost and Effectiveness for Deteriorated Bridge Substructure Repair."

Wipf, T. J., Fanous, F., Klaiber, F., and Eapen, A. (2003). "Evaluation of Appropriate Maintenance, Repair and Rehabilitation Methods for Iowa Bridges." *Final Report, Iowa DOT Project TR-429*.

Xia, M., Nematollahi, B., and Sanjayan, J. (2019). "Printability, accuracy and strength of geopolymer made using powder-based 3D printing for construction applications." *Automation in Construction*, 101, 179-189.

Xia, M., Nematollahi, B., and Sanjayan, J. G. (2019). "Properties of Powder-Based 3D Printed Geopolymers." *3D Concrete Printing Technology*, Elsevier, 265-280.

Zhang, Y., Zhang, Y., Liu, G., Yang, Y., Wu, M., and Pang, B. (2018). "Fresh properties of a novel 3D printing concrete ink." *Construction and building materials*, 174, 263-271.

VITA

Fareh Waleed Abudawaba grew up in Ma'an, Jordan. She earned her Bachelor of Science in Civil Engineering from Al-Hussein Bin Tala University in Ma'an, Jordan in August 2015. In May 2021, she earned her master of science in Civil Engineering from Missouri University of Science and Technology in Rolla, Missouri. Following graduation, she was accepted into the Ph.D. program.